Mon. Not. R. Astron. Soc. **356,** 1308–1326 (2005) doi:10.1111/j.1365-2966.2004.08556.x

Probing the wind–wind collision in γ^2 Velorum with high-resolution *Chandra* X-ray spectroscopy: evidence for sudden radiative braking and non-equilibrium ionization

David B. Henley,[1]★ Ian R. Stevens[1] and Julian M. Pittard[2]

[1]*School of Physics and Astronomy, University of Birmingham, Edgbaston, Birmingham B15 2TT*
[2]*School of Physics and Astronomy, University of Leeds, Woodhouse Lane, Leeds LS2 9JT*

Accepted 2004 October 25. Received 2004 October 20; in original form 2004 May 11

ABSTRACT

We present a new analysis of an archived *Chandra* HETGS X-ray spectrum of the WR+O colliding wind binary γ^2 Velorum. The spectrum is dominated by emission lines from astrophysically abundant elements: Ne, Mg, Si, S and Fe. From a combination of broad-band spectral analysis and an analysis of line flux ratios we infer a wide range of temperatures in the X-ray-emitting plasma (∼4–40 MK). As in the previously published analysis, we find the X-ray emission lines are essentially unshifted, with a mean FWHM of 1240 ± 30 km s^{-1}. Calculations of line profiles based on hydrodynamical simulations of the wind–wind collision predict lines that are blueshifted by a few hundred km s^{-1}. The lack of any observed shift in the lines may be evidence of a large shock-cone opening half-angle (>85°), and we suggest this may be evidence of sudden radiative braking. From the *R* and *G* ratios measured from He-like forbidden-intercombination-resonance triplets we find evidence that the Mg XI emission originates from hotter gas closer to the O star than the Si XIII emission, which suggests that non-equilibrium ionization may be present.

Key words: stars: individual: γ^2 Velorum – stars: winds, outflows – stars: Wolf–Rayet – X-rays: stars.

1 INTRODUCTION

γ^2 Velorum (WR 11, HD 68273) is the closest known Wolf–Rayet (WR) star, at a *Hipparcos*-determined distance of 258^{+41}_{-31} pc (Schaerer, Schmutz & Grenon 1997). As such, it is a key system for increasing our understanding of X-ray emission from massive early-type stars. γ^2 Vel is a double-lined spectroscopic binary of spectral type WC8 + O7.5 (de Marco & Schmutz 1999) whose orbit is well determined, with a period of 78.53 ± 0.01 d, $e = 0.326 \pm 0.01$, $\omega_{\rm WR} = 68 \pm 4^\circ$ (Schmutz et al. 1997) and $i = 63 \pm 8^\circ$ (de Marco & Schmutz 1999).

In a system consisting of a WR star with an early-type companion, a substantial contribution to the X-ray emission should come from the collision of the stars' dense, highly supersonic winds (Cherepashchuk 1976). However, the situation is complicated by the fact that the individual stars may also have substantial intrinsic X-ray emission from shocks that develop in the winds as a result of line-driven instabilities (e.g. Owocki, Castor & Rybicki 1988). An important signature of colliding wind emission is phase-locked variability of the flux and/or hardness of the X-ray emission. The simplest explanation for the variability of these observable quantities is the variation in the amount of absorption the X-rays suffer as the system moves through its orbit. Increasing absorption reduces the flux, but it also increases the hardness because softer X-rays are more strongly absorbed. In an eccentric binary, there may be other factors that give rise to phase-locked variability. Near periastron, the intrinsic X-ray luminosity may increase because the winds are denser when they collide. The emission will also be softer if the winds are not travelling at their terminal velocities, as the shock speeds will be slower near periastron compared with apastron.

Einstein observations of γ^2 Vel found that it was not unusually bright in X-rays, with $L_{\rm X}/L_{\rm bol(O)} = 0.44 \times 10^{-7}$ (Pollock 1987) (cf. the mean $L_{\rm X}/L_{\rm bol}$ for single stars in the *Einstein* catalogue of O stars, which is 2.5×10^{-7} – Chlebowski 1989; see also Moffat et al. 2002). There was however a suggestion that the X-rays from γ^2 Vel are softer when the O star is in front of the WR star (Pollock 1987).

The first convincing evidence of the wind–wind collision in γ^2 Vel came not from X-ray data, but from *International Ultraviolet Explorer* (*IUE*) and *Copernicus* ultraviolet spectra (St-Louis, Willis & Stevens 1993). They found that in broad terms the variability of the UV line profiles could be explained in terms of selective line eclipses of the O star light by the WR star wind, with the

★E-mail: dbh@star.sr.bham.ac.uk

effect being restricted to resonance and low-excitation transitions of species common in the WC8 wind (e.g. C II, C III, C IV, Si III, Si IV and S IV). However, the details of some of the variability could not be explained by a simple spherically symmetric WR star wind. Instead there was evidence from resonance lines expected to occur in the winds of both stars (C IV, Si IV and S IV) that the collision between the stars' winds forms a cavity in the WR star wind. At phases when the O star is in front, one is looking into the cavity and sees the O star wind in absorption. As the O star wind is $\sim$1000 km s^{-1} faster than the WR star wind, a high-velocity blue absorption wing appears in the P Cygni profile. At phases when the WR star is in front, the O star wind travelling towards the observer is prevented from reaching its terminal velocity by the wind–wind collision, and so the high-velocity wing disappears, masked by the absorption trough of the WR star wind.

X-ray emission from the wind–wind collision in γ^2 Vel was first studied in detail with *ROSAT*. From an analysis of 13 observations, Willis, Schild & Stevens (1995) found significant phase-dependent X-ray variability that is repeatable with binary phase. They found two main components to the emission. When the O star was not in front of the WR star, the emission in the 0.1–2.5 keV range was relatively constant and soft ($kT \sim 0.19$ keV) with $L_{\rm X} \sim 2.5 \times 10^{31}$ erg s^{-1}. When the O star was in front they found the X-ray emission was enhanced by the addition of a harder component, with $kT \gtrsim$ 1–2 keV and $L_{\rm X} \gtrsim 10^{32}$ erg s^{-1}. They attributed this harder component to emission from the wind–wind collision, observed through the cavity in the WR star wind formed by the O star wind. This was supported by hydrodynamical modelling of the wind–wind collision, which found that at *ROSAT* energies the emission from the wind–wind collision is only observable at phases when the O star is in front. Using the winds' terminal velocities in the hydrodynamical simulations overpredicted the luminosity in the *ROSAT* band (0.1–2.5 keV) by about an order of magnitude. Better agreement with the observations was obtained by assuming the O star wind collided at less than its terminal velocity, which is expected as the wind–wind collision region is likely to be close to the O star (because its wind is much weaker than that of the WR star).

The hydrodynamical modelling in Willis et al. (1995) predicted copious X-ray emission at energies greater than 2.5 keV, inaccessible by *ROSAT*, but within the range of *ASCA*. Stevens et al. (1996) obtained two *ASCA* spectra taken near periastron (at phases $\Phi =$ 0.978 and $\Phi = 0.078$, where $\Phi = 0$ corresponds to periastron). These were compared with a set of synthetic X-ray spectra, generated from hydrodynamical simulations with a range of different wind parameters (namely the mass-loss rates and terminal velocities of the two winds). By fitting their synthetic spectra to their observed spectra, Stevens et al. (1996) were not only able to confirm the conclusion of Willis et al. (1995) that γ^2 Vel is a colliding wind system, but were also able to put constraints on some of the stars' wind parameters. Most notably, they found the mass-loss rate of the WR star to be $\sim 3 \times 10^{-5}$ M$_\odot$ yr^{-1}. This is a factor of three lower than the mass-loss rate derived from radio observations (8.8×10^{-5} M$_\odot$ yr^{-1} according to Barlow, Roche & Aitken 1988). Stevens et al. (1996) suggest this may be because radio observations tend to overestimate mass-loss rates if the wind is inhomogeneous.

Rauw et al. (2000) analysed an additional *ASCA* spectrum of γ^2 Vel, this time near apastron ($\Phi = 0.570$), and also reanalysed the data in Stevens et al. (1996). Having taken into account background sources, Rauw et al. (2000) effectively fitted the hard variable emission with a single temperature model. The bulk of the variability can be attributed to a changing column density towards the source. However, the temperature and luminosity also vary. The $\Phi = 0.978$ spectrum has a lower temperature ($kT \sim 1.9$ keV, using non-solar abundances) than the $\Phi = 0.570$ spectrum ($kT \sim 2.7$ keV). This could be because near apastron the winds are moving more quickly when they collide, resulting in a larger post-shock temperature. The softest (and intrinsically most luminous) spectrum is seen at $\Phi =$ 0.078 ($kT \sim 1.3$ keV). If the soft X-rays are from the wind–wind collision, then at this phase they are being seen through the cavity in the WR star wind caused by the wind collision (whose position has been deflected by the Coriolis force). Alternatively, it could indicate that the intrinsic emission from the O star wind is making a significant contribution. In either case, at the other two phases the soft emission is absorbed by the wind of the WR star.

The unprecedented spectral resolution offered by the *Chandra* Low- and High-Energy Transmission Grating Spectrometers (LETGS and HETGS) and the *XMM–Newton* Reflection Grating Spectrometer ($E/\Delta E \sim$ 100–1000) give us the opportunity to measure X-ray line shifts and widths to accuracies down to a few hundred km s^{-1}. This enables us to probe in detail the dynamics of the X-ray-emitting plasma in colliding wind binaries, giving new insights into the structure of the wind–wind interaction regions in such systems.

We present a new analysis of an archived *Chandra* HETGS observation of γ^2 Vel. These data have already been analysed by Skinner et al. (2001). They found that the X-ray emission lines were broadened (FWHM $\sim$ 1000 km s^{-1}) but unshifted from their rest wavelengths. Furthermore, their results imply that the Ne IX line emission originates tens of stellar radii from the O star, well away from the central wind–wind collision region near the line of centres. Our analysis includes a larger number of emission lines than published by Skinner et al. (2001). We also discuss in more detail the interpretation of our results in terms of a colliding wind picture. The details of the observation and the data reduction are described in Section 2. The broad-band spectral properties are described in Section 3, while the results of fitting to the individual emission lines are described in Section 4. In Section 5 we describe our attempts to model the emission line profiles using the model of Henley, Stevens & Pittard (2003). Our results are discussed in Section 6 and summarized in Section 7. Throughout this paper, the quoted errors are 1σ confidence ranges.

2 OBSERVATION AND DATA REDUCTION

γ^2 Vel was observed by the *Chandra* HETGS between 2000 March 15 09:20:04 UT and 2000 March 16 04:08:12 UT, giving 64 848 s of useful exposure time. The observation covered orbital phases $\Phi = 0.080$–0.090, where $\Phi = 0$ corresponds to periastron passage, using the ephemeris of Schmutz et al. (1997):

$$\mathrm{JD(periastron)} = 245\,0120.5 + 78.53E, \quad (1)$$

where E is the number of orbits since the periastron passage on JD 245 0120.5. Mid-observation was 6.7 d after periastron, and about 4 d after the passage of the O star in front of the WR star ($\Phi = 0.03$). The separation of the stars during the observation was 0.92–0.94 au (assuming $M_{\rm WR} = 9.5$ M$_\odot$ and $M_{\rm O} = 30$ M$_\odot$ – see de Marco & Schmutz 1999; de Marco et al. 2000).

The dispersed photons from the *Chandra* HETGS grating assembly form a shallow X in the focal plane (see Fig. 1). One 'arm' of the X is from the High-Energy Grating (HEG), the other is from the Medium-Energy Grating (MEG). The HEG has higher spectral resolution than the MEG: $\Delta\lambda = 12$ mÅ FWHM over the range 1.2–15 Å for the HEG, versus $\Delta\lambda = 23$ mÅ FWHM over the range

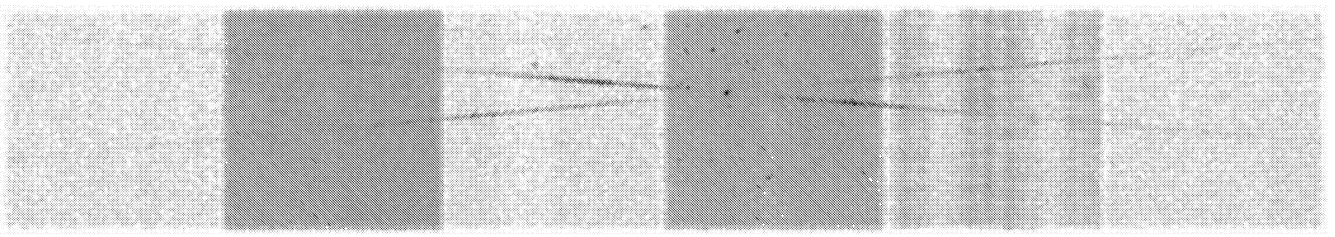

Figure 1. The *Chandra* ACIS-S detector showing the dispersed photons of the HETGS spectrum of γ^2 Vel. One arm of the X is from the HEG, the other is from the MEG. For the purposes of this figure, the data have been binned up by a factor of 16 to exaggerate the grating arms, and the image has been rotated so the ACIS-S detector is horizontal.

2.5–31 Å for the MEG (*Chandra* Proposers' Observatory Guide,[1] Section 8.1). On the other hand, the MEG gives a higher signal-to-noise ratio in the first-order spectra of γ^2 Vel.

The data were reduced from the Level 1 events file using CIAO v3.1, following threads available from the *Chandra* website.[2] This was done in preference to using the spectrum file obtained from the *Chandra* archive because it meant a more up-to-date version of CALDB (v2.27) could be applied to the data. Similarly, response files (ARFs and RMFs) appropriate for this observation were generated following *Chandra* threads, in preference to using 'off-the-shelf' response files.

There are a total of 7850 counts in the non-background-subtracted first-order HEG spectrum and 16 003 counts in the non-background-subtracted first-order MEG spectrum. For the analysis described here, the data were not background subtracted, nor was the background spectrum modelled separately. For each of the two HETGS gratings, the background counts are extracted from two regions either side of and 4.5 times as wide as the source-extraction regions (which are 4.8-arcsec wide in the cross-dispersion direction). There is therefore a possibility that photons from bright spectral lines could spread out into the background-extraction regions (because of the point-spread function of the telescope). Indeed, there is some evidence that the brighter emission lines in the source spectrum are also in the background spectrum. This means that background subtraction could adversely affect the measured results. Furthermore, the Cash statistic, which was used for the analysis of emission lines described in Section 4, cannot be used with background-subtracted data. However, the count rates in the background-extraction regions are less than 1 per cent of the rates in the corresponding source-extraction regions (taking into account the fact that the background counts come from a detector area nine times larger than the source counts).

3 BROAD-BAND SPECTRAL PROPERTIES

The HEG and MEG spectra of γ^2 Vel are shown in Fig. 2. For illustrative purposes, the $+1$ and -1 orders have been co-added, and the spectra have been binned up to 0.02 Å. The spectrum of γ^2 Vel is dominated by strong emission lines from S ($\lambda \approx 4$–5 Å), Si ($\lambda \approx 5$–7 Å) and Mg ($\lambda \approx 7$–9 Å), with weaker lines from Ne ($\lambda \approx 9$–14 Å) and Fe (e.g. $\lambda \approx 2$ Å and $\lambda \approx 10$ Å). In this section we describe the analysis of the global properties of the spectrum, while in the following section we describe our analysis of the individual emission lines.

The broad-band spectral analysis was carried out using XSPEC[3] v11.3.1. For the purposes of this analysis, the $+1$ and -1 orders of each spectrum were co-added, and the data were binned so there were at least 20 counts per bin. This meant that the χ^2 statistic could be used, and the goodness of various spectral models could be assessed. The spectral models were fitted to the HEG and MEG spectra simultaneously, using all the available data.

The ARFs used in the broad-band spectral fitting were generated by co-adding the ARFs for the relevant $+1$ and -1 orders. A similar procedure cannot be followed for the RMFs, and so one must use the RMF for either the $+1$ or -1 order for the whole co-added spectrum. Experimentation showed that the combination of HEG and MEG RMFs used did not have a significant effect on the results. However, it was noted that the value of χ^2 obtained when using the HEG -1 RMF and the MEG $+1$ RMF was always lower than when using any of the other three possible combinations. The differences in χ^2 were always small, but this may be connected with the fact that the HEG -1 order and the MEG $+1$ order contain the larger number of counts in their respective spectra – 3951 counts (HEG -1) versus 3899 counts (HEG $+1$) and 8543 counts (MEG $+1$) versus 7460 counts (MEG -1). The results described hereinafter were obtained using this pair of RMFs.

3.1 2*T* models

A visual inspection of the *Chandra* HETGS spectrum of γ^2 Vel indicates there is a wide range of temperatures present in the X-ray-emitting plasma, as evidenced by emission lines from a wide range of ions – from Ne IX, whose emission peaks at $T_{\max} \approx 4$ MK ($kT_{\max} = 0.34$ keV), to S XVI, whose emission peaks at $T_{\max} \approx 25$ MK ($kT_{\max} = 2.2$ keV). Hydrodynamical simulations of the wind–wind collision also predict a wide range of temperatures (see Section 5). One would therefore not expect a 2*T* thermal plasma model to provide a good fit to the spectrum; at best it can only characterize the emission, rather than accurately describe in detail the temperature structure of the X-ray-emitting gas. Furthermore, because of the wealth of detail in a grating spectrum (as opposed to a CCD spectrum), a plasma-emission model may have difficulty accurately fitting all the emission lines. The problems that arise could be due to several factors: Doppler shifting of lines, line broadening (on top of thermal Doppler broadening and instrumental broadening), non-solar abundances, and inaccurate atomic physics parameters (such as transition rates and lab wavelengths) in the plasma emission model. Nevertheless, with these caveats in mind, fitting a 2*T* model to the spectrum of γ^2 Vel can give some insight into the general properties of the X-ray-emitting plasma. For this purpose, we used the

[1] http://cxc.harvard.edu/proposer/POG/index.html
[2] http://cxc.harvard.edu/ciao/threads/gspec.html
[3] http://heasarc.gsfc.nasa.gov/docs/xanadu/xspec/

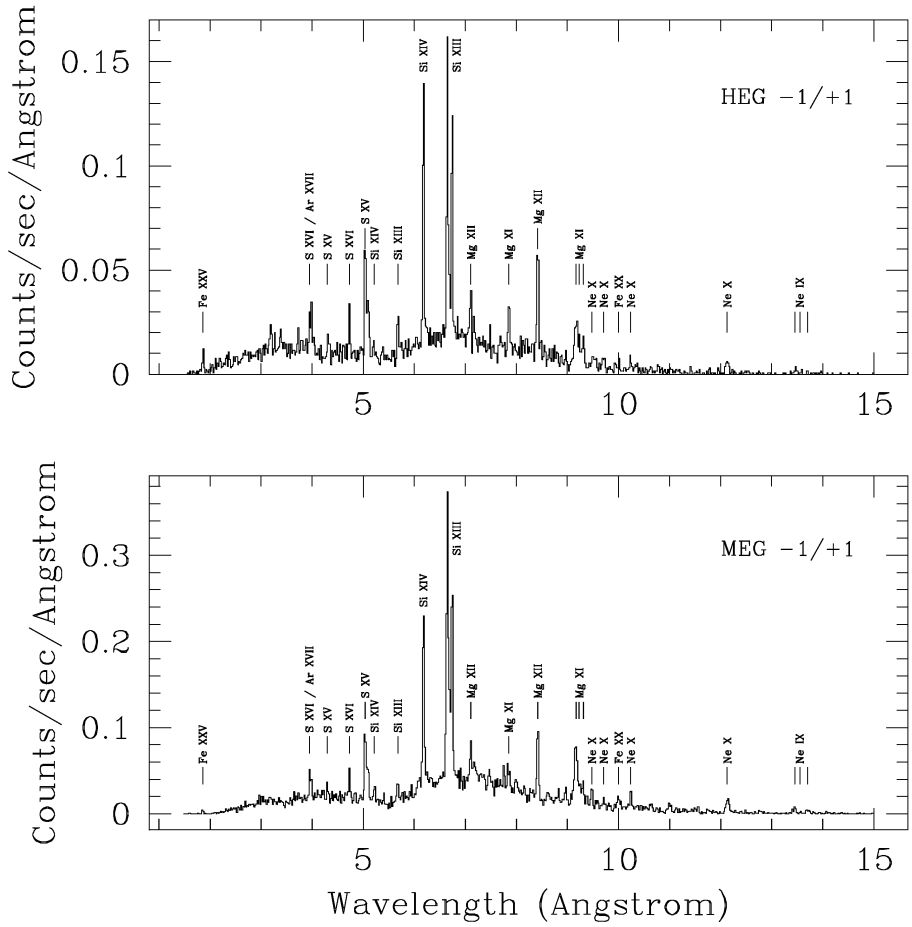

Figure 2. The first-order HEG and MEG spectra of γ^2 Velorum. The +1 and −1 orders have been co-added, and the spectra binned up to 0.02 Å.

XSPEC `apec` model (Astrophysical Plasma Emission Code;[4] Smith & Brickhouse 2000; Smith et al. 2001). To model the absorption by the stellar winds we used the XSPEC `wabs` model (which uses cross-sections from Morrison & McCammon 1983).

We expect a significant portion of the X-ray emission to originate from the wind–wind interaction region, which is an approximately conical region around the O star whose apex points along the line of centres towards the WR star. The hot shocked gas streams along this cone away from the apex. At the time of the *Chandra* observation, the O star was approximately in front of the WR star, and hence the opening of the shock cone was towards the observer. There was therefore hot gas streaming along the shock cone towards the observer, and so we would expect to observe blueshifted emission lines. Because the opening of the shock cone was not directly towards the observer, there would in fact have been a range of line-of-sight velocities (distributed azimuthally around the shock cone), and so we would also expect to observe broadened emission lines. This simple picture of the X-ray emission from the wind–wind collision is developed further in Section 4.5.

The amount of Doppler shifting and Doppler broadening of the X-ray emission lines can be determined to a certain degree from the broad-band spectrum (though this is done in more detail by investigating the individual lines; see Section 4). Line Doppler shifts can be modelled by thawing the `apec` model's redshift parameter z. Note that this parameter measures the line-of-sight velocity of the X-ray-emitting plasma, not the systemic line-of-sight velocity (as the shocked gas is moving with respect to the stars). Line broadening can be modelled by using the XSPEC `gsmooth` model, which convolves the whole spectrum with a Gaussian. The standard deviation σ of this Gaussian can vary as a power-law with photon energy E:

$$\sigma(E) = \sigma_6 \left(\frac{E}{6\ \mathrm{keV}} \right)^{\alpha}, \qquad (2)$$

where σ_6 is the standard deviation at 6 keV. However, in practice it was found that thawing the index α did not significantly improve the fit, so it was frozen at 1 (which gives a constant linewidth expressed as a velocity). For the fitting, one `gsmooth` component was used for the whole spectrum, and also the redshifts of the two `apec` models were constrained to be equal (so there is one redshift characterizing the whole spectrum).

We used non-solar abundances in our fitting, using the XSPEC `vapec` model. This model calculates abundances relative to hydrogen, which is essentially absent in WR winds. We overcame this by setting a large helium abundance – $N(\mathrm{He})/N(\mathrm{H}) = 10^6$, where $N(\mathrm{X})$ denotes the number abundance of element X – and then measuring abundances relative to helium. The abundances of C, N and O were fixed at $N(\mathrm{C})/N(\mathrm{He}) = 0.14$ (Morris et al. 1999; Schmutz & de Marco 1999), $N(\mathrm{N})/N(\mathrm{He}) = 1.0 \times 10^{-4}$ (Lloyd & Stickland 1999) and $N(\mathrm{O})/N(\mathrm{He}) = 0.028$ (from $N(\mathrm{C})/N(\mathrm{O}) = 5$; de Marco et al. 2000). Furthermore, as a starting point we used $N(\mathrm{Ne})/N(\mathrm{He})$

[4] http://cxc.harvard.edu/atomdb/sources_apec.html

Table 1. Results of fitting the *Chandra* HETGS spectrum of γ^2 Vel with an absorbed two-temperature thermal plasma model (models A and B: `wabs*gsmooth*(vapec+vapec)`) and an absorbed differential emission measure thermal plasma model (model C: `wabs*gsmooth*c6pvmkl` – see Section 3.2). Model A has σ_6 (see equation 2) and the redshift frozen at 0; in models B and C they are free parameters. The emission measures are expressed in terms of the helium number density $n_{\rm He}$ (EM $= \int n_{\rm e} n_{\rm He}\,{\rm d}V$), because of the lack of hydrogen in the WR star wind. The quoted abundances are number ratios, relative to the solar number ratios (Anders & Grevesse 1989). The X-ray luminosities are for the 0.4–10 keV energy range.

Model	A	B	C
$N_{\rm H}$ (10^{22} cm^{-2})	1.92 ± 0.04	2.08 ± 0.03	$2.24^{+0.07}_{-0.04}$
kT_1 (keV)	$0.773^{+0.012}_{-0.014}$	$0.763^{+0.010}_{-0.009}$	–
EM$_1$ (10^{54} cm^{-3})	2.29 ± 0.08	$2.28^{+0.03}_{-0.15}$	–
kT_2 (keV)	$2.19^{+0.08}_{-0.05}$	$2.15^{+0.04}_{-0.05}$	–
EM$_2$ (10^{54} cm^{-3})	1.07 ± 0.05	$0.96^{+0.07}_{-0.03}$	–
σ_6 (eV)	0 (frozen)	$10.6^{+0.2}_{-0.4}$	$9.3^{+0.3}_{-0.4}$
Redshift z (km s^{-1})	0 (frozen)	$-18.3^{+0.9}_{-1.4}$	-160^{+10}_{-14}
(Ne/He)/(Ne/He)$_\odot$	0.98 ± 0.12	$1.81^{+0.19}_{-0.18}$	$1.53^{+0.17}_{-0.16}$
(Mg/He)/(Mg/He)$_\odot$	0.53 ± 0.03	$1.09^{+0.05}_{-0.04}$	$1.13^{+0.04}_{-0.06}$
(Si/He)/(Si/He)$_\odot$	$0.85^{+0.02}_{-0.03}$	1.34 ± 0.03	$1.24^{+0.03}_{-0.05}$
(S/He)/(S/He)$_\odot$	1.17 ± 0.07	$1.66^{+0.07}_{-0.08}$	1.50 ± 0.07
(Fe/He)/(Fe/He)$_\odot$	0.55 ± 0.06	$0.99^{+0.06}_{-0.05}$	$0.68^{+0.06}_{-0.05}$
χ^2_ν (d.o.f.)	2.81 (919)	1.78 (917)	1.95 (914)
$L_{\rm X}^{\rm abs}$ (10^{32} erg s^{-1})	1.0	1.1	1.1
$L_{\rm X}^{\rm int}$ (10^{32} erg s^{-1})	6.7	8.4	–

$= 3.5 \times 10^{-3}$ and $N({\rm S})/N({\rm He}) = 6 \times 10^{-5}$ (Dessart et al. 2000), and we fixed the relative abundances of all elements heavier than neon at their solar values (Anders & Grevesse 1989). From this starting point, we allowed the abundances of Ne, Mg, Si, S and Fe to vary.

The results of fitting the *Chandra* HETGS spectrum of γ^2 Vel with an absorbed two-temperature thermal plasma model with non-solar abundances – `wabs*gsmooth*(vapec+vapec)` – are shown in Table 1. Model A has σ_6 and z frozen at 0, whereas in model B they are both free parameters. The data and the best-fitting models (concentrating on the S and Si line region) are shown in Figs 3 (model A) and 4 (model B). Thawing σ_6 and z significantly improves χ^2, although the fit is still formally unacceptable (the reduced χ^2 is 1.78 for 917 degrees of freedom). Figs 3 and 4 indicate that the poor fits are mainly due to the emission lines, rather than the continuum. Nevertheless, the derived parameters can give us an overview of the general properties of the X-ray-emitting plasma. The two temperatures derived from the fit (≈9 and 25 MK) are sensible given the range of peak emission temperatures of the lines observed in the spectrum. The value of σ_6 corresponds to a FWHM of 1250^{+20}_{-50} km s^{-1}. The small measured line shift ($z = -18$ km s^{-1}) implies the lines are not systematically shifted from their rest wavelengths. The values of σ_6 and z can be compared with the results of fitting to individual emission lines (see Section 4.2). Thawing σ_6 and z does not affect the temperatures and emission measures of the two components. Also, while it seems significantly to affect the column density $N_{\rm H}$, this is probably not the case because the errors in Table 1 are likely to be underestimated (given the poorness of the fits).

While the abundances for a given model in Table 1 seem well constrained, a comparison between models indicates that this is in fact not the case. Furthermore, some measurements are hampered by the fact that for some elements only a few lines are available to constrain the abundance. For example, the neon abundance is really only being determined from the Ne X Lyα and Lyβ lines, and this will lead to a temperature–abundance degeneracy. Indeed, uncertainties in the temperature distribution will affect all the abundance determinations. Unfortunately, this therefore means that the abundances in Table 1 are rather unreliable.

Note that the X-ray luminosities in Table 1 have been derived using the *Hipparcos*-determined distance of 258^{+41}_{-31} pc (Schaerer et al. 1997). This result has recently been thrown into doubt by the serendipitous discovery of an association of low-mass pre-main sequence (PMS) stars in the direction of γ^2 Vel (Pozzo et al. 2000). Pozzo et al. (2000) argue that these PMS stars are at approximately the same distance and age as γ^2 Vel, placing γ^2 Vel within the Vela OB2 association at a distance of 360–490 pc, in good agreement with older distance estimates (e.g. 460 pc; Conti & Smith 1972). If this larger distance is correct, the X-ray luminosities in Table 1 should be increased by a factor of ∼3.

The absorbing column $N_{\rm H}$ derived from the fit corresponds to a visual extinction $A_v \approx 9$, using the empirical relation of Gorenstein (1975). In contrast, the visual extinction derived from optical studies is $A_v = 0.00$–0.12 (van der Hucht 2001). This implies that there is extra absorption local to the source, in addition to the interstellar absorption. Given the orientation of the orbit and the phase of the observation, the wind–wind collision zone was observed through the wind of the O star. The value of $N_{\rm H}$ is consistent with the column density through the wind of the O star to a point in the wind–wind collision zone that lies on the line of centres, which may reasonably be assumed to be a characteristic column density for the whole emission region. This can be shown by considering the optical depth τ_ν through a spherically symmetric wind expanding at constant velocity v_∞ to a point at (r, θ, ϕ) (in spherical coordinates centred on the star, with the z-axis along the line of sight), which is given by (Ignace 2001)

$$\tau_\nu = \tau_\star \frac{R_\star}{r} \frac{\theta}{\sin\theta}, \tag{3}$$

where $R_\star$ is the stellar radius and $\tau_\star = \kappa_\nu \dot{M}/4\pi v_\infty R_\star$ is a characteristic wind optical depth (Owocki & Cohen 2001), where $\dot{M}$ is the stellar mass-loss rate and κ_ν is the opacity. The optical depth is related to the column density $N_{\rm H}$ by

$$\tau_\nu = \int \kappa_\nu \rho \,{\rm d}r \approx \int \kappa_\nu m_{\rm H} n_{\rm H} \,{\rm d}r = \kappa_\nu m_{\rm H} N_{\rm H}, \tag{4}$$

where ρ is the mass density, $n_{\rm H}$ is the number density of hydrogen and $m_{\rm H}$ is the mass of a hydrogen atom. Thus, by combining equations (3) and (4), we obtain

$$N_{\rm H} = \frac{\dot{M}}{4\pi m_{\rm H} v_\infty r} \frac{\theta}{\sin\theta}. \tag{5}$$

The angle θ, i.e. the polar angle (in this coordinate system) of a point on the line of centres, is related to the orbital phase angle Ψ ($\Psi = 0^\circ$ corresponding to the O star being in front) and the orbital inclination i by

$$\cos\theta = -\cos\Psi \sin i. \tag{6}$$

(See also equation 4 in Henley et al. (2003); note that the θ used in that equation is the supplement of the θ in equations 3 and 5.) Using the orbital elements of Schmutz et al. (1997) ($e = 0.326$, $\omega_{\rm WR} = 68^\circ$) and the phase of the *Chandra* observation ($\Phi = 0.085$ at mid-observation; see Section 2), we obtain $\Psi = 36^\circ$. Combining this with $i = 63^\circ$ (de Marco & Schmutz 1999) gives $\theta = 136^\circ$. Using the separation (≈0.93 au) and the wind momentum ratio

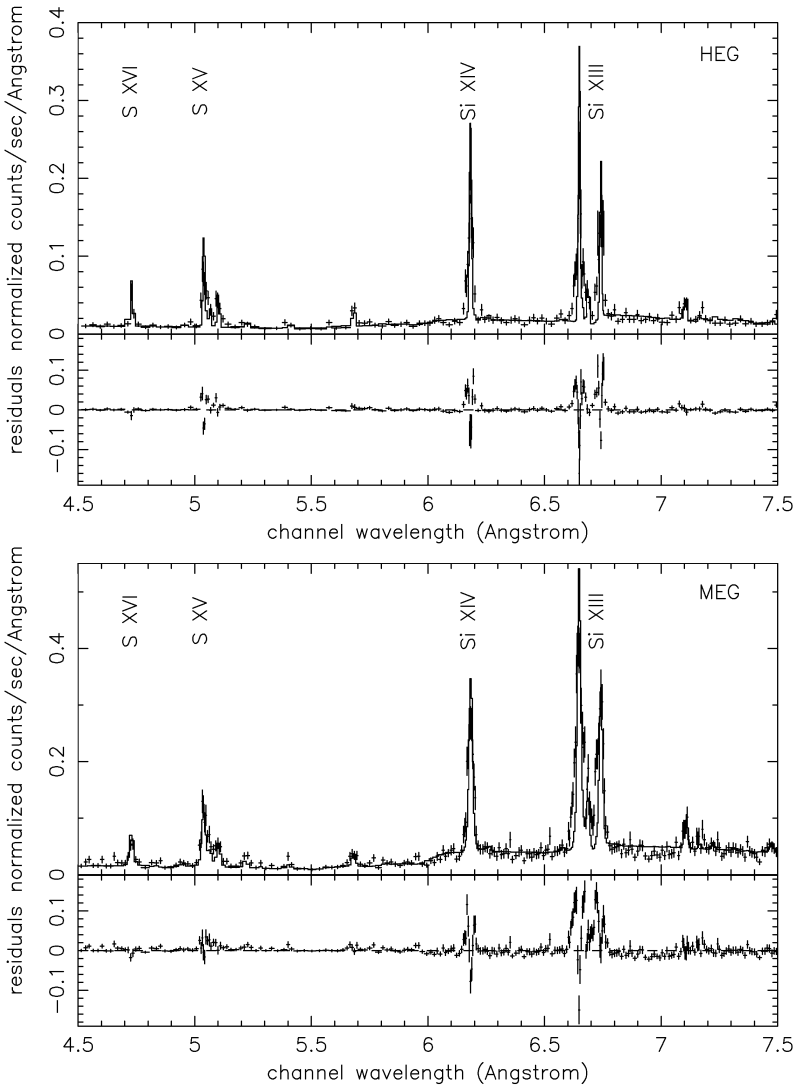

Figure 3. The binned HEG (top) and MEG (bottom) spectra from γ^2 Vel plotted with the best-fitting absorbed $2T$ `apec` model, with the redshift z and σ_6 frozen at 0 (model A in Table 1). The residuals are the direct differences between the data and the model (in normalized counts s^{-1} $Å^{-1}$).

($\dot{M}_{\rm WR} v_{\rm WR} / \dot{M}_{\rm O} v_{\rm O} \approx 33$; de Marco et al. 2000), the distance along the line of centres from the O star to the wind–wind collision zone is $r \approx 2 \times 10^{12}$ cm. The mass-loss rate and wind velocity are more difficult to determine, and the situation is complicated by the fact that the wind will not be at its terminal velocity at the wind collision. One consequence of this is that the column density will be larger than that given by equation (5), because the inner regions of the wind are denser than is assumed by a constant-expansion model. Assuming $\dot{M} = 0.1\text{–}1 \times 10^{-6}\,{\rm M}_\odot\,{\rm yr}^{-1}$ and $v_\infty = 2000$ km s^{-1} (which are sensible values for a late O star), we find $N_{\rm H} \approx 0.3\text{–}3 \times 10^{22}$ cm^{-2}, which is consistent with the values derived from spectral fitting. However, it should be noted that the `wabs` absorption model in XSPEC assumes neutral absorbing material. This will overestimate the opacity of the partially ionized stellar wind, and so underestimate $N_{\rm H}$. This discrepancy will be worst at lower energies ($\lesssim 1$ keV; see fig. 4 in Cohen et al. 1996).

If we invert the above argument, and specify our measured value of $N_{\rm H}$ in equation (5), we obtain $\dot{M}_{\rm O} \sim 8 \times 10^{-7}\,{\rm M}_\odot\,{\rm yr}^{-1}$. However, this value may not be very reliable, given the approximations used to obtain it.

3.2 DEM modelling

As has already been stated, a $2T$ `apec` model can only characterize the spectrum, rather than accurately describing the temperature structure of the X-ray-emitting plasma. One would expect to obtain a more detailed picture of the temperature structure by using a differential emission measure (DEM) model.

Skinner et al. (2001) fitted the first-order MEG spectrum of γ^2 Vel with an absorbed differential emission measure (DEM) model, and found a strong emission measure peak near ~9–10 MK. We attempted to reproduce this, using a `wabs*gsmooth*c6pvmkl` model in XSPEC. This model is based on the `mekal` thermal plasma model (unfortunately there is no DEM model in XSPEC based on `apec`). The DEM is expressed as an exponential of a polynomial:

$$\mathrm{DEM}(T) \propto \exp\left[\sum_{k=1}^{6} a_k P_k(T)\right], \qquad (7)$$

where P_k is a Chebyshev polynomial of order k, and the coefficients a_k are free to vary during the fit. As in the previous

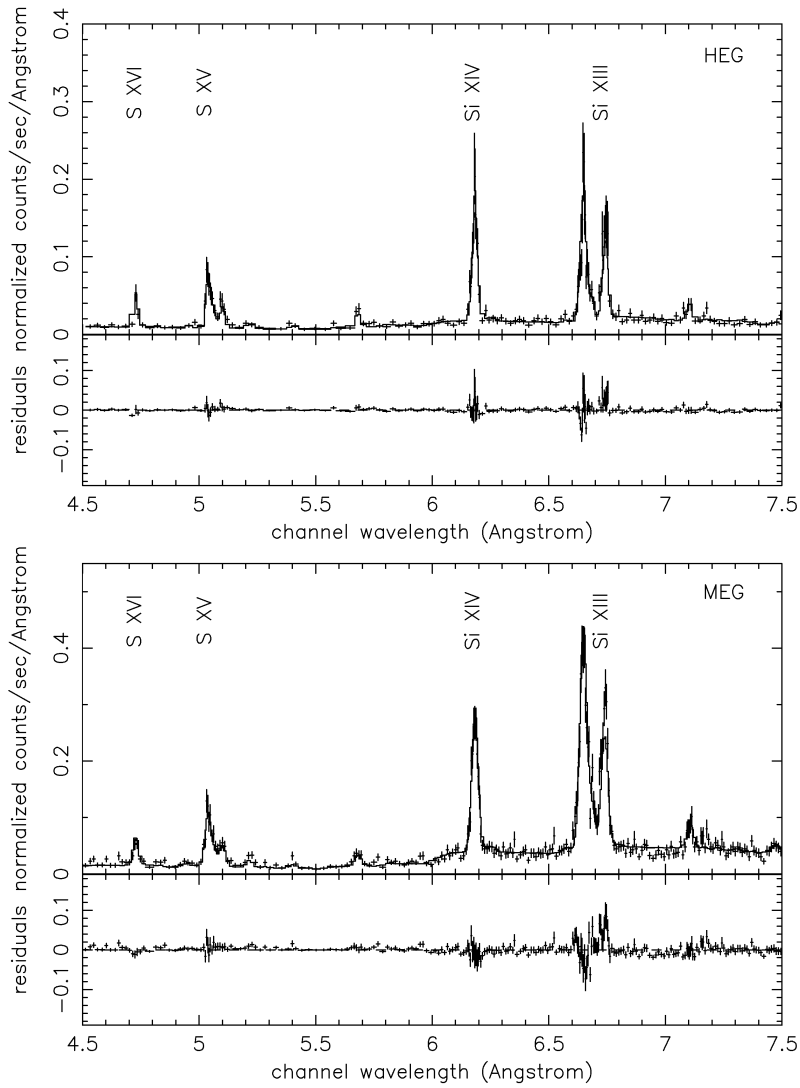

Figure 4. As Fig. 3, but with the redshift z and σ_6 free to vary (model B in Table 1).

section, the abundances of Ne, Mg, Si, S and Fe were free parameters, as were σ_6 and z. Again, we fitted the HEG and MEG spectra simultaneously.

Our best-fitting DEM is shown in Fig. 5, and the resulting spectral parameters are in Table 1 (model C). The DEM `mekal` model actually gives a worse fit than the $2T$ `apec` model. This is most probably due to the fact that `mekal` is an older code, and so may have inaccurate wavelengths, transition rates, etc. compared with the more up-to-date `apec` model. This means the derived spectral parameters should be treated with caution (in particular the redshift z, which is significantly different from that obtained in Section 3.1).

Our DEM is broadly peaked at ∼7–8 MK, compared with the strong peak at ∼10 MK found by Skinner et al. (2001). To estimate the uncertainty in the shape of the DEM, we have calculated the errors in the coefficients a_k using XSPEC, and then used these in a Monte Carlo simulation to generate a set of 1000 DEMs. While the small peak at ∼35 MK does not seem to be very significant, the drops in the DEM below 7 MK and above 40 MK do seem to be real. The DEM therefore indicates a wide range of plasma temperatures from a few MK to ∼40 MK, as expected from the range of emission lines seen in the spectrum. Without knowing more about

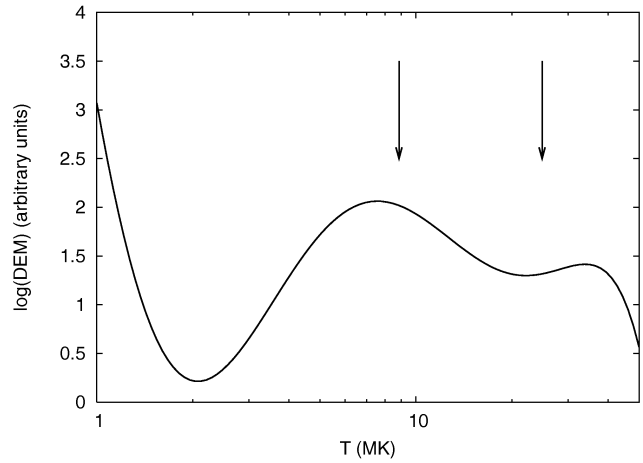

Figure 5. Our best-fit differential emission measure (DEM) model for γ^2 Vel. The arrows (at 8.85 and 24.9 MK) indicate the best-fit temperatures from our $2T$ `apec` model fitting (Table 1, model B). The rise in the DEM below ∼2 MK is probably an artefact of the assumed functional form of the DEM (equation 7).

Skinner et al.'s (2001) DEM, we cannot say whether or not our DEM is consistent with theirs.

An alternative method of calculating the DEM (with uncertainties) would be to use the method described by Wojdowski & Schulz (2004), which involves fitting the spectrum with a number of components, each of which is the entire X-ray emission line spectrum for a single ion. The DEM is thus pieced together from the emission measures of these individual components (each of which corresponds to a different temperature range). However, such an additional analysis of the DEM is beyond the scope of this paper.

Rather surprisingly, our DEM also shows a pronounced rise below ∼2 MK. However, as there is very little emission above ∼14 Å, the cool end of the DEM (below ∼4 MK, the peak emission temperature of Ne IX) will be very poorly constrained. This rise in the DEM is thus almost certainly just an artefact of the assumed functional form of the DEM (equation 7). An unfortunate consequence of the rise in the DEM at low temperatures is that the intrinsic (unabsorbed) flux is over-estimated by several orders of magnitude at low energies. For this reason we have not quoted a value for $L_{\rm X}^{\rm int}$ for this model in Table 1. This excessive intrinsic low-energy flux probably explains why the column density derived from the DEM model is somewhat higher than that derived from the 2T model (see Table 1).

4 EMISSION LINE PROPERTIES

Unlike the broad-band spectral analysis, the analysis of the individual lines in the *Chandra* spectrum of γ^2 Vel was carried out using unbinned, non-co-added spectra, so no spectral information was lost. Because some bins contained low numbers of counts, the Cash statistic (Cash 1979) was used instead of χ^2. This analysis was carried out using SHERPA (as distributed with CIAO v3.1).

The analysis of the X-ray spectrum concentrated on the emission lines from H- and He-like ions of Ne, Mg, Si and S. For all four of these elements the H-like Lyα lines and He-like f.i.r. (forbidden-intercombination-resonance) triplets were detected. Lyβ lines were also analysed for Ne X, Mg XII and Si XIV, but not S XVI, as its Lyβ line is blended with the Ar XVII f.i.r. triplet near 3.95 Å. The Ne X Lyman series extends to include Lyγ and Lyδ. Heβ lines (1 s3p ^{1}P$_1$ → 1s^2 ^{1}S$_0$) were also detected from Si XIII and Mg XI.

Each emission line or multiplet was analysed individually over a narrow range of wavelengths (typically 0.2–0.5 Å). The fitted model consisted of a continuum component plus Gaussian component(s) to model the line emission. Although colliding wind binaries are expected to exhibit a wide range of line profile shapes (Henley et al. 2003), Gaussians give good fits to the emission lines in γ^2 Vel (see Section 4.1), and thus provide a good way of quantifying the line shifts and widths. It was found that the choice of continuum model (constant or power-law) did not significantly affect the best-fit parameters of line emission component. As a result the simpler constant model was chosen in preference. The nature of the line emission component used depended on the nature of the line being investigated, as discussed below.

Lyman lines are in fact closely spaced doublets owing to the spin–orbit splitting of the upper level. The splitting is ≈5 mÅ for Lyα and ≈1 mÅ for Lyβ. This separation is too small to be resolved by the *Chandra* gratings, and so a good fit can be obtained with a single Gaussian. However, it is not obvious what should be used as the rest wavelength of the line if one wishes to measure a Doppler shift. The Lyman lines were therefore fitted with two Gaussians whose parameters were tied together. The Doppler shifts of the two components (expressed as velocities) were constrained to be equal, as were their widths. The relative intensities of the two components were fixed at the theoretical values from ATOMDB v1.1.0, the shorter-wavelength component being approximately twice as bright as the longer-wavelength component.

In contrast to the Lyman lines, the components of the He-like f.i.r. triplets are resolvable by the *Chandra* gratings. These lines were fitted with three Gaussians whose parameters were tied together (the intercombination line is in fact a closely spaced doublet, but using four Gaussians did not significantly alter the results). The Doppler shifts and widths were linked as for the Lyman lines. For this purpose, the laboratory wavelength of the brighter, longer-wavelength intercombination line was used. The amplitudes of the Gaussians were all free to vary. The Heβ lines are singlets, and so these were fitted with single Gaussians.

4.1 Fits to individual lines

The fit results are shown in Table 2. All these results were obtained by fitting the line model to all four spectra (HEG −1 and +1, MEG −1 and +1) simultaneously, except for the S XVI Lyα line (the results were obtained just from the MEG data, as a sensible fit could not be obtained if the HEG data were included) and the Si XIV Lyα line (the MEG −1 data were excluded from the fit; see below). For each individual spectrum the appropriate ARF and RMF was used.

The Lyα lines and He-like f.i.r. triplets from S, Si, Mg and Ne are shown in Fig. 6, along with the best-fitting model for each. For illustrative purposes only the data have been binned up to 0.01 Å in these plots. For comparison, the unbinned S XV f.i.r. triplet and Si XIV Lyα line are shown in Fig. 7. Note that there appears to be some excess emission in the S XV f.i.r. HEG data approximately 0.01 Å shortwards of the forbidden line. However, this is probably not real, because it does not appear at the same wavelength in the +1 and −1 orders, it does not appear at all in the MEG data, and there is no corresponding feature shortwards of the resonance line. Note also that the MEG −1 Si XIV Lyα line appears significantly different from the others – it is shifted towards the red, and also it appears to be skewed redwards. However, this skewing is probably not real – if it were it should be detected in the other three spectra (if anything, the line in the MEG +1 spectrum appears to be slightly skewed bluewards). The wavelength obtained by fitting to just the MEG −1 spectrum is 6.1834 ± 0.0014 Å, that obtained by fitting to the other three spectra is 6.1795 ± 0.0006 Å, and that obtained by fitting to all four spectra is 6.1803 ± 0.0006 Å. Hence, while the MEG −1 spectrum gives a significantly different wavelength from the other three spectra, including it in the fit does not significantly affect the results (this is true of the FWHM and flux as well). Nevertheless, as the line is clearly different in the MEG −1 spectrum, we have chosen to quote the results obtained by omitting the MEG −1 spectrum from the fit in Table 2.

The fit results are illustrated in Fig. 8, which shows the measured line shifts and widths as functions of laboratory wavelength. One can see from the results that the lines are typically unshifted from their lab wavelengths, with FWHMs of ∼1000–1500 km s^{-1}. The shifts and widths are uncorrelated with lab wavelength or the ionization potential of the emitting ion. The line shifts are well fitted with a single mean shift (independent of wavelength) of −64 ± 12 km s^{-1}($\chi^2_\nu = 1.13$ for 14 degrees of freedom), while the linewidths are adequately fitted with a single mean FWHM of 1240 ± 30 km s^{-1} ($\chi^2_\nu = 1.91$ for 14 degrees of freedom).

While the Cash statistic can be used on data with low numbers of counts, it does not contain any goodness-of-fit information. Therefore, to get some idea of the goodness of the fits, we again co-added

Table 2. The measured wavelengths (λ_{obs}), widths ($\Delta\lambda$) and fluxes of the X-ray emission lines in the *Chandra* HETGS spectrum of γ^2 Vel. All results were obtained by fitting to the unbinned, non-co-added HEG and MEG spectra simultaneously (except where indicated). Parameters without quoted errors were tied to other fit parameters, rather than being free. Laboratory wavelengths (λ_{lab}) and temperatures of maximum emission (T_{max}) are from ATOMDB v1.1.0.

Ion	Line	kT_{max} (keV)	λ_{lab} (Å)	λ_{obs} (Å)	FWHM $\Delta\lambda$ (Å)	FWHM $\Delta\lambda$ (km s^{-1})	Observed flux (10^{-5} photons cm^{-2} s^{-1})
S XVI[a]	Lyα_1	2.165	4.7274	4.7289 ± 0.0020	0.0115 ± 0.0068	730 ± 430	1.92 ± 0.36
	Lyα_2	2.165	4.7328	4.7343	0.0115	730	0.92
S XV	He *r*	1.366	5.0387	5.0382 ± 0.0010	0.0203 ± 0.0020	1210 ± 120	8.60 ± 0.69
	He *i*	1.085	5.0665	5.0660	0.0205	1210	2.71 ± 0.51
	He *f*	1.366	5.1015	5.1010	0.0206	1210	4.15 ± 0.50
Si XIV	Lyβ_1	1.366	5.2168	5.2168 ± 0.0036	0.026 ± 0.010	1510 ± 570	1.28 ± 0.38
	Lyβ_2	1.366	5.2180	5.2179	0.026	1510	0.61
Si XIII	Heβ	0.862	5.6805	5.6800 ± 0.0018	0.0199 ± 0.0047	1050 ± 250	2.45 ± 0.40
Si XIV[b]	Lyα_1	1.366	6.1804	6.1795 ± 0.0006	0.0237 ± 0.0015	1150 ± 73	5.94 ± 0.25
	Lyα_2	1.366	6.1858	6.1849	0.0237	1150	2.84
Si XIII	He *r*	0.862	6.6479	6.6459 ± 0.0004	0.0287 ± 0.0010	1295 ± 45	12.23 ± 0.42
	He *i*	0.862	6.6882	6.6862	0.0289	1295	3.13 ± 0.28
	He *f*	0.862	6.7403	6.7383	0.0291	1295	7.98 ± 0.32
Mg XII	Lyβ_1	0.862	7.1058	7.1049 ± 0.0019	0.0247 ± 0.0077	1040 ± 230	0.94 ± 0.14
	Lyβ_2	0.862	7.1069	7.1060	0.0247	1040	0.45
Mg XI	Heβ	0.544	7.8503	7.8521 ± 0.0035	0.0407 ± 0.0075	1550 ± 290	1.11 ± 0.22
Mg XII	Lyα_1	0.862	8.4192	8.4169 ± 0.0010	0.0291 ± 0.0028	1036 ± 89	2.97 ± 0.21
	Lyα_2	0.862	8.4246	8.4223	0.0291	1036	1.42
Mg XI	He *r*	0.544	9.1687	9.1636 ± 0.0020	0.0501 ± 0.0042	1640 ± 140	3.63 ± 0.29
	He *i*	0.544	9.2282	9.2261	0.0505	1640	1.23 ± 0.22
	He *f*	0.544	9.3143	9.3091	0.0509	1640	1.20 ± 0.21
Ne X	Lyδ_1	0.544	9.4807	9.4810 ± 0.0033	0.0263 ± 0.0081	830 ± 260	0.45 ± 0.10
	Lyδ_2	0.544	9.4809	9.4812	0.0263	830	0.22
Ne X	Lyγ_1	0.544	9.7080	9.7095 ± 0.0050	0.0414 ± 0.0099	1280 ± 310	0.41 ± 0.11
	Lyγ_2	0.544	9.7085	9.7100	0.0414	1280	0.20
Ne X	Lyβ_1	0.544	10.2385	10.2393 ± 0.0029	0.0319 ± 0.0080	930 ± 230	0.70 ± 0.13
	Lyβ_2	0.544	10.2396	10.2404	0.0319	930	0.34
Ne X	Lyα_1	0.544	12.1321	12.1331 ± 0.0032	0.0594 ± 0.0075	1470 ± 190	1.84 ± 0.23
	Lyα_2	0.544	12.1375	12.1385	0.0595	1470	0.89
Ne IX	He *r*	0.343	13.4473	13.4530 ± 0.0043	0.0594 ± 0.0098	1320 ± 220	1.54 ± 0.32
	He *i*	0.343	13.5531	13.5589	0.0599	1320	0.38 ± 0.19
	He *f*	0.343	13.6990	13.7048	0.0605	1320	1.00 ± 0.27

[a]Results obtained just by fitting to MEG data.
[b]Results obtained by omitting MEG −1 data from the fit.

the +1 and −1 orders of the HEG and MEG spectra, binned up the data so there were at least 10 counts per bin, and then repeated the fitting procedure using χ^2 (which does enable us to assess the goodness of fit). Just for this χ^2 fitting, the HEG −1 and MEG +1 RMFs were used, as in the broad-band spectral fitting. To illustrate the effect of rebinning the data, the binned Si XIV Lyα line is shown in Fig. 9. We found no significant difference in the wavelengths, widths and fluxes derived using the two different fit statistics – all agreed within 1 σ. In all cases, Gaussians give good fits to the emission lines. A possible exception to this is the Si XIII f.i.r. triplet – Gaussians do not give good fits to the HEG lines (which appear to be slightly skewed redwards) but they do to the MEG lines. However, this skewing is probably not real, as there is no evidence for it in the MEG data (which has higher signal-to-noise). There is therefore no convincing evidence that Gaussian line profiles do not give good fits to the observed emission lines.

There is no improvement in χ^2 when two Gaussians are used for the Lyman lines as opposed to just one. However, while it is not required by the data, the use of a doublet model is justified on physical grounds, as discussed above.

4.2 Comparison with broad-band results

The results described in this section can be compared with the results derived from the broad-band spectrum in Section 3.1. Fig. 10 compares the line shifts and widths derived in this section with those inferred from the values of z and σ_6 in Table 1 (model B). There is excellent agreement between the width derived from the broad-band fitting (FWHM $= 1250^{+20}_{-50}$ km s^{-1}) and the mean width of the individual emission lines (FWHM $= 1240 \pm 40$ km s^{-1}). Furthermore, the lack of any observed correlation between linewidth and wavelength justifies our use of $\alpha = 1$ in equation (2).

We would expect there to be good agreement between the line shifts derived from the broad-band fitting and the mean shift of the individual emission lines, as the rest wavelengths in the `tapec` model used to measure the former are the same as those used to calculate the latter. In fact, the line shift derived from the broad-band fitting ($z = -18.3^{+0.9}_{-1.5}$ km s^{-1}) disagrees with the mean shift of the individual emission lines (-64 ± 12 km s^{-1}) at the 3σ level. However, the agreement is probably better than this indicates, because the poor spectral fits in Section 3 mean the

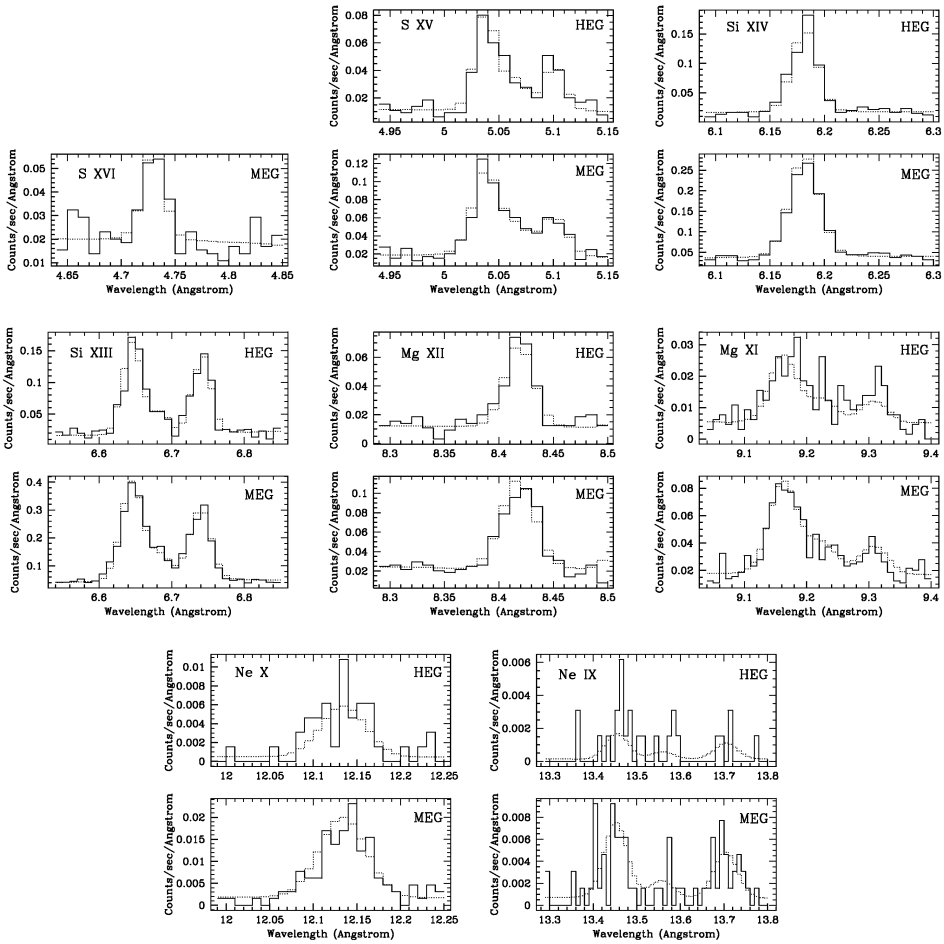

Figure 6. The Lyα lines from S XVI, Si XIV, Mg XII and Ne X and the He-like f.i.r. triplets from S XV, Si XIII, Mg XI and Ne IX observed in the *Chandra* HETGS spectrum of γ^2 Vel. The solid line in each panel shows the data, while the dashed line shows the best-fit model. For illustrative purposes only, the $+1$ and -1 orders of each grating (HEG and MEG) have been co-added and binned up to 0.01 Å. Note that the S XVI Lyα fit was just carried out on the MEG data, and so the HEG data are not plotted.

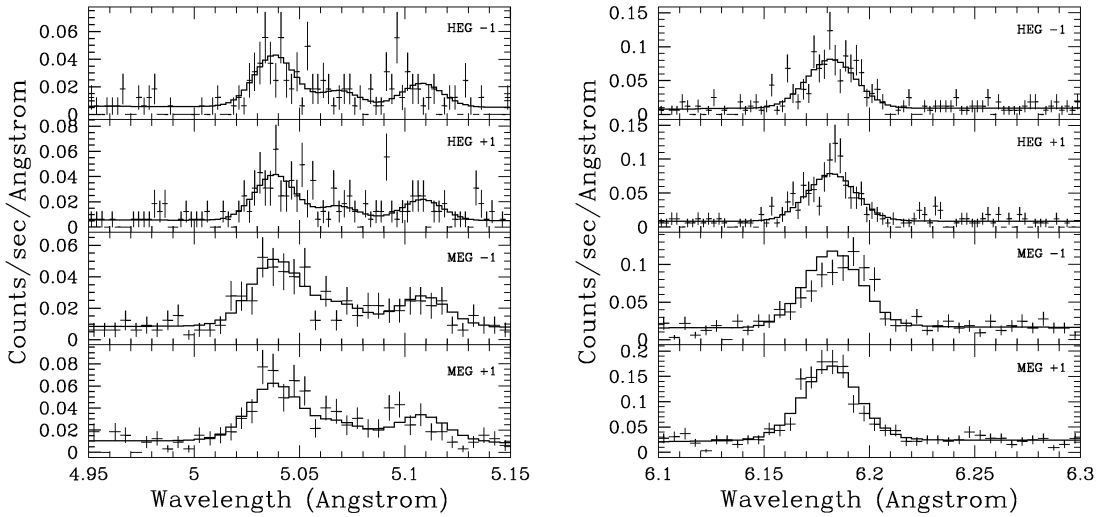

Figure 7. The unbinned S XV f.i.r. triplet (left) and Si XIV Lyα line (right), with the best-fit Gaussian line profiles. The anomalous appearance of the MEG -1 line in the right figure is discussed in the text.

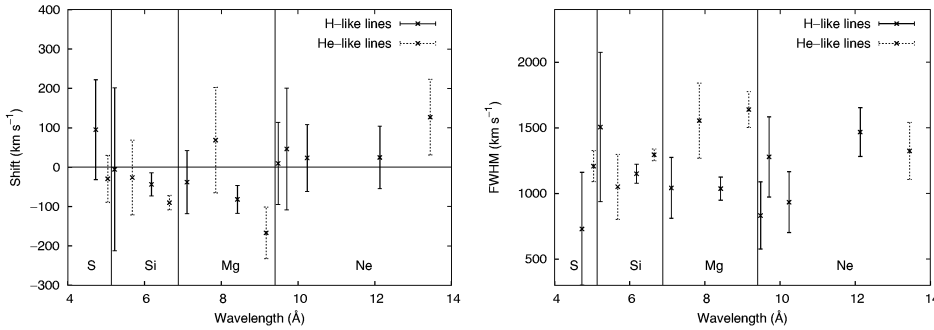

Figure 8. Line shifts (left) and widths (right) as functions of laboratory wavelength. The vertical lines divide the plot up into lines from S, Si, Mg and Ne (from left to right). Lines from H-like and He-like ions are denoted with solid and dashed error bars, respectively.

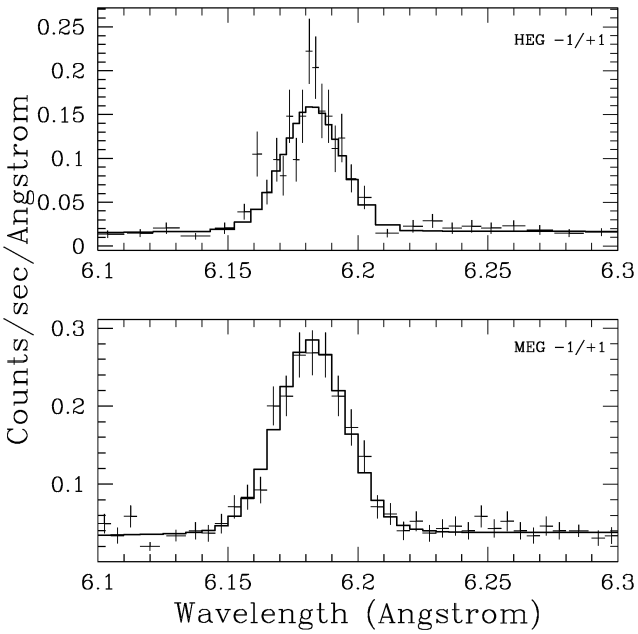

Figure 9. The Si XIV Lyα line shown binned up so there are at least 10 counts per bin, with the best-fit Gaussian line profile, obtained by fitting to the two binned spectra simultaneously using χ^2.

errors in the spectral parameters (including z) are likely to be underestimated.

4.3 Estimating the temperature using line flux ratios

There are two simple ways to estimate the temperature T of the X-ray-emitting plasma using the flux ratios of emission lines. The first uses the flux ratio of the H-like Lyα line to the He-like resonance line for a given element. As the temperature increases the ionization balance shifts from He- to H-like ions, and this change is manifested in the line flux ratio. The second uses the flux ratio $G = (f + i)/r$ of the resonance (r; 1s2p ^{1}P$_1$ $\rightarrow$ 1s^2 ^{1}S$_0$), intercombination (i; 1s2p ^{3}P$_{1,2}$ $\rightarrow$ 1s^2 ^{1}S$_0$) and forbidden (f; 1s2s ^{3}S$_1$ $\rightarrow$ 1s^2 ^{1}S$_0$) lines of a He-like ion. G is a decreasing function of temperature (e.g. Porquet et al. 2001; Paerels & Kahn 2003), due to the different temperature dependencies of the mechanisms for populating the upper levels of the lines (direct collisional excitation from the ground state for the resonance line, cascades from higher levels populated by dielectronic recombination for the forbidden and intercombination lines; see Smith et al. 2001). The G ratio is also sensitive to electron density at high densities, owing to population of the upper level of the resonance line from the 1s2s ^{1}S$_0$ level (Porquet et al. 2001). However, the densities at which this becomes important ($n_e \gtrsim 10^{12}$ cm^{-3}; Porquet et al. 2001) are larger than those expected in the wind–wind collision in γ^2 Vel (the hydrodynamical simulations in Section 5 indicate $n_e \lesssim 10^{11}$ cm^{-3}).

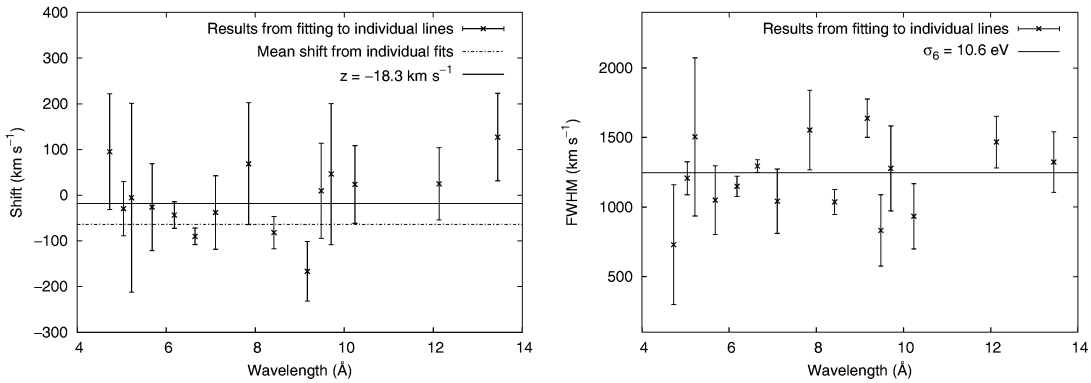

Figure 10. Comparison between line shifts (left) and linewidths (right) derived from fitting to the broad-band spectrum and those derived from fitting to individual emission lines. The data points in both figures are the results from fitting to individual emission lines. The dot–dashed line in the top figure shows the mean shift of the lines (-64 km s^{-1}). The solid line in the top figure shows the line shift corresponding to $z = -18.3$ km s^{-1}, and the solid line in the bottom figure shows the linewidth corresponding to $\sigma_6 = 10.6$ eV (model B, Table 1).

To estimate temperatures using H-like to He-like flux ratios, we use line emissivities calculated as functions of T with the Astrophysical Plasma Emission Code and Data base (APEC/APED;[5] Smith & Brickhouse 2000; Smith et al. 2001). These emissivities are distributed in ATOMDB v1.1.0. Comparing the measured H-like to He-like flux ratios with the calculated values, we infer temperatures of 5.6 ± 0.5 MK for Ne, 8.6 ± 0.3 MK for Mg, 11.7 ± 0.2 MK for Si and 14 ± 1 MK for S.

The measured G ratios are 0.9 ± 0.3, 0.67 ± 0.10 and 0.91 ± 0.05 for Ne IX, Mg XI and Si XIII, respectively. To calculate temperatures, we compare these values to the values calculated by Porquet et al. (2001) in the low-density limit. Their calculations include the effects of blending of dielectronic satellite lines. The contribution of these blended lines to the measured fluxes depends on the spectral resolution of the instrument used (Porquet et al. 2001), and so they tabulate G ratios as a function of T assuming the MEG spectral resolution ($\Delta\lambda$ (FWHM) = 23 mÅ) and assuming the HEG spectral resolution ($\Delta\lambda$ = 12 mÅ). Our fits use data from the MEG and the HEG simultaneously. However, this does not matter as there are no significant differences between the temperatures inferred using the MEG values or the HEG values from Porquet et al. (2001). Using the MEG values from Porquet et al. (2001) we infer temperatures of 3^{+3}_{-2} MK for Ne IX, 7^{+3}_{-2} MK for Mg XI and $4.8^{+0.8}_{-0.7}$ MK for Si XIII, whereas using the HEG values we infer 2^{+4}_{-2} MK for Ne IX, 7^{+3}_{-2} MK for Mg XI and $5.4^{+0.8}_{-0.7}$ MK for Si XIII.

The temperatures measured using the f.i.r. triplets of Ne IX and Mg XI are in good agreement with those measured using the H-like to He-like flux ratios. However, the temperature measured from the Si XIII f.i.r. triplet is significantly cooler than that measured from the Si XIV:Si XIII flux ratio. The calculation of the temperature from the G ratio may be affected by blending of the Si XIII forbidden line with Mg XII Lyγ. This would mean the G ratio is over-estimated and T is under-estimated by this method, in agreement with the observed discrepancy. However, the discrepancy may more simply be due to the He-like emission coming from different, cooler regions than the H-like emission.

4.4 The location of the X-ray-emitting plasma

The flux ratio $R = f/i$ is sensitive both to electron density n_e and the UV radiation field, owing to depopulation of the upper level of the forbidden line to the upper level of the intercombination line (Gabriel & Jordan 1969; Porquet et al. 2001; Paerels & Kahn 2003). Comparing the measured R ratios with theoretical values gives information on the electron density and/or UV radiation field, and with some other assumptions the location of the X-ray-emitting plasma can be inferred.

The measured R ratios are 2.6 ± 1.5 for Ne, 1.0 ± 0.2 for Mg and 2.5 ± 0.2 for Si. Porquet et al. (2001) have calculated R ratios as functions of n_e for a range of electron temperatures, radiation temperatures and radiation dilution factors ($W(r) = 0.5[1-\sqrt{1-(R_*/r)^2}]$, where r is the distance from the centre of a star of radius R_*). The radius of the WR star is 3.2 $R_\odot$ (de Marco et al. 2000), and the distance from the WR star to the wind–wind interaction will be at least half the separation (i.e. $r > 100$ $R_\odot$). The dilution factor of the WR star's radiation field is thus $W < 0.00026$, and its effect on the observed R ratios will be negligible.

Fig. 11 shows the R ratio as a function of n_e in the absence of a radiation field ($T_{rad} = 0$), and in the presence of a blackbody radiation field with $T_{rad} = 35\,000$ K (the effective temperature of the O star; de Marco & Schmutz 1999) for two different values of the dilution factor, calculated by averaging the data for 30 000 and 40 000 K in Porquet et al. (2001). The plotted curves are for electron temperatures of 3.0 MK (Ne IX), 6.3 MK (Mg XI) and 5.0 MK (Si XIII). These temperatures were chosen from the values tabulated by Porquet et al. (2001) based on the values derived in using G ratios in Section 4.3, though in fact the choice of electron temperature has no effect on the conclusions. Also shown in Fig. 11 are the measured R ratios.

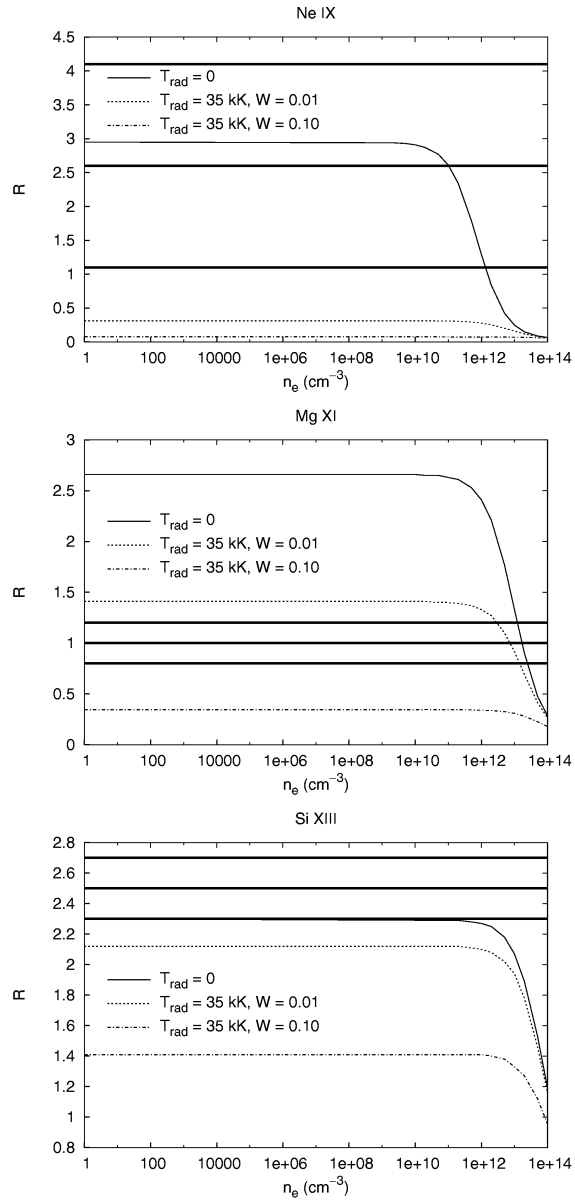

Figure 11. Measured and calculated R ratios for Ne IX, Mg XI and Si XIII. The thin curves show the R ratio as a function of n_e for different radiation temperatures (T_{rad}) and dilution factors (W). The thick horizontal lines show the measured R ratios and the 1σ errors.

For Ne IX, the observed value of the R ratio is consistent with the theoretical low-density, low-UV flux value ($R \approx 3$). Furthermore, we can see that even a relatively weak UV flux ($W \sim 0.01$) would give rise to an R ratio significantly lower than that which is observed. We therefore conclude that $W \ll 0.01$. The radius of the O star is

[5] http://cxc.harvard.edu/atomdb/

12.4 $R_\odot$ (de Marco & Schmutz 1999), and hence for the Ne IX-emitting plasma, $r \gg 5R_*(\mathrm{O}) = 4 \times 10^{12}$ cm. By the same argument, we can see from Fig. 11 that $W < 0.01$ for Si XIII, and so we have $r > 5R_*(\mathrm{O})$ for the Si XIII-emitting plasma.

For Mg XI the observed value of the R ratio is significantly lower than the theoretical low-density, low-UV flux value ($R \approx 2.7$). If the UV radiation field were negligible, this would imply an electron density of $\sim 10^{13}$ cm^{-3}, which is far larger than is expected in the wind–wind collision zone. Even with a dilution factor of $W \sim 0.01$, the implied density ($\sim 10^{12}$–10^{13} cm^{-3}) is too large. On the other hand, if the dilution factor were as large as $W \sim 0.10$, the value of the R ratio would be significantly lower than that which is observed. Hence for the Mg XI-emitting plasma, $0.01 < W < 0.10$, and so $1.7R_*(\mathrm{O}) < r < 5R_*(\mathrm{O})$. This means the Mg XI emission emerges from closer to the O star than the Si XIII emission. The implications of this are discussed in Section 6. It should be noted, however, that the uncertainty in the O star's emergent photospheric flux at the far- and extreme-ultraviolet wavelengths relevant for the photoexcitation transitions (1270 Å for Ne IX, 1033 Å for Mg XI and 864 Å for Si XIII; Porquet et al. 2001) may be significant, and that a 35 000 K blackbody does not represent the flux of the O star very well, especially at the wavelengths relevant to the higher Z elements. A more accurate model of the photospheric flux would probably modify the curves in Fig. 11 in a way that is not easy to predict.

Skinner et al. (2001) use this data set to derive distances of the X-ray-emitting plasma from the O star by considering the following relationship between the R ratio, the electron density n_e and the UV photoexcitation rate ϕ from the fth to the ith upper levels:

$$R = \frac{R_0}{1 + (\phi/\phi_\mathrm{c}) + (n_\mathrm{e}/n_\mathrm{c})}, \tag{8}$$

where n_c is the critical density and ϕ_c the critical photoexcitation rate (Blumenthal, Drake & Tucker 1972). R_0 is the low-density, low-UV flux limit of the R ratio, i.e. if $n_\mathrm{e} \ll n_\mathrm{c}$ and $\phi \ll \phi_\mathrm{c}$, $R \rightarrow R_0$. Skinner et al. (2001) argue that $R \geqslant \frac{2}{3}R_0$ for their f.i.r. triplets (as lower values of the R ratio would be unambiguously detected), and hence $\phi/\phi_\mathrm{c} \leqslant 0.5$. Using the results of Blumenthal et al. (1972), they derive minimum line formation radii of $r_\mathrm{min} \approx 3R_*(\mathrm{O}), 9R_*(\mathrm{O})$ and $30R_*(\mathrm{O})$ for Si XIII, Mg XI and Ne IX, respectively. Their results for Si XIII and Ne IX are consistent with our results. Using the more recent results of Porquet et al. (2001) instead of Blumenthal et al. (1972), we have increased r_min for Si XIII from $3R_*(\mathrm{O})$ to $5R_*(\mathrm{O})$. On the other hand, our analysis does not place a strong constraint on r_min for Ne IX, mainly because Porquet et al. (2001) do not quote values of the R ratio for dilution factors below 0.01.

It is not surprising that Ne IX originates far from the O star. Near the line of centres (and hence near the O star) the winds collide head-on, producing shock-heated plasma that is too hot for Ne IX to exist (tens of MK). This plasma moves outwards along the shock-cone, cooling radiatively. It will not cool to the temperature at which Ne IX emission peaks (≈4 MK) until it has travelled some distance (the hydrodynamical simulations discussed in Section 5 indicate the plasma cools to ≈4 MK at a distance of $\approx 10R_*(\mathrm{O})$ from the O star). This is a factor of three less than the minimum line formation radius derived by Skinner et al. (2001). However, an inspection of the models used in Section 3.1 shows that there is considerable iron emission near the Ne IX f.i.r. triplet; combined with the fact that there are very few counts in this part of the spectrum, this means the Ne IX results are probably untrustworthy.

Our results for the location of the Mg XI-emitting plasma are different from those of Skinner et al. (2001). We find this plasma is located at $1.7R_*(\mathrm{O}) < r < 5R_*(\mathrm{O})$, whereas Skinner et al. (2001) derive $r > 9R_*(\mathrm{O})$. Part of this discrepancy may come from the fact we measure different values of the R ratio for Mg XI: $1.8^{+0.9}_{-0.5}$ (Skinner et al. 2001) versus 1.0 ± 0.2 (this work). This difference may be due to differences in the calibration used, or to the fact that Skinner et al. (2001) use background-subtracted HEG data only, whereas we use data from both gratings without background subtraction. It should be noted that our measured width for the Mg XI f.i.r. triplet is significantly larger than most of the other widths in Table 2. In order to assess whether or not this affects our flux measurements, we have repeated the fit with the triplet's FWHM fixed at 1200 km s^{-1} (the average FWHM of all the lines). These measured fluxes are ∼10–20 per cent lower than our original measured values, but the differences are not significant. Furthermore, the R ratio is unaffected.

Skinner et al. (2001) further state that uncertainties in their flux measurements and possible blending with Ne X Lyman lines means that their value of the Mg XI R ratio could be consistent with the low-density limit R_0. The Ne X Lyman lines from upper levels 6–10 have wavelengths of 9.362, 9.291, 9.246, 9.215 and 9.194 Å, respectively (Huenemoerder, Canizares & Schulz 2001), whereas the wavelengths of the Mg XI forbidden and intercombination lines are 9.314 and 9.231 Å (ATOMDB v1.1.0). Given the wavelengths of these Ne X lines, and without any information on their emissivities (these lines are not in APED), it is difficult to say which (the f line or i line) will be more affected by blending, and hence one cannot say for sure that the measured value of the R ratio for Mg XI is probably underestimated.

If we do assume that blending with Ne X Lyman lines tends to lower the observed value of the R ratio for Mg XI, we can derive a location for the Mg XI-emitting plasma using the method in Skinner et al. (2001). However, whereas they used $R \geqslant \frac{2}{3}R_0$, given our results we can only say that $R \geqslant \frac{1}{3}R_0$. This implies $\phi/\phi_\mathrm{c} \leqslant 2.0$, and gives $r > 4.5R_*(\mathrm{O})$, which is consistent with the range we derive above using the Porquet et al. (2001) data.

4.5 Geometry of the wind–wind collision

Some insight into the geometry of the wind–wind collision zone may be gained by assuming the X-ray line emission comes from a cone with opening half-angle β whose symmetry axis lies along the line of centres with the apex pointing towards the WR star (Lührs 1997; Pollock et al. 2004). This arrangement is illustrated in Fig. 12. The angle γ between the line of centres and the line of sight is the supplement of the angle θ in equation (6) and hence is given by $\cos\gamma = \cos\Psi \sin i$. We assume the emitting material is flowing along the cone at speed v_0 and that there is no azimuthal velocity component (these are explicit assumptions of the model due to Lührs 1997). The former is justified in the light of 2-D hydrodynamical simulations of the colliding winds (such as those in Section 5), which show that the velocity vector is indeed directed along the shock cone. There is a small divergence in the velocity, but this will not have a significant effect. The latter assumption is justified because an azimuthal velocity component in the post-shock gas will require one to be present in the pre-shock gas, and this will not be the case in a radially outflowing wind.

With these assumptions, the centroid shift ($\bar{v}$) and velocity range ($v_\mathrm{max} - v_\mathrm{min}$) of an emission line are given by (Lührs 1997; Pollock et al. 2004)

$$\bar{v} = -v_0 \cos\beta \cos\gamma \tag{9}$$

$$v_\mathrm{max} - v_\mathrm{min} = 2\Delta v = 2v_0 \sin\beta \sin\gamma. \tag{10}$$

In particular, $\bar{v}$ comes from 'Term 1' in Lührs's equation (9), where his $\phi^\star$ equals our Ψ and his v_WR equals our v_0, while Δv is equal to

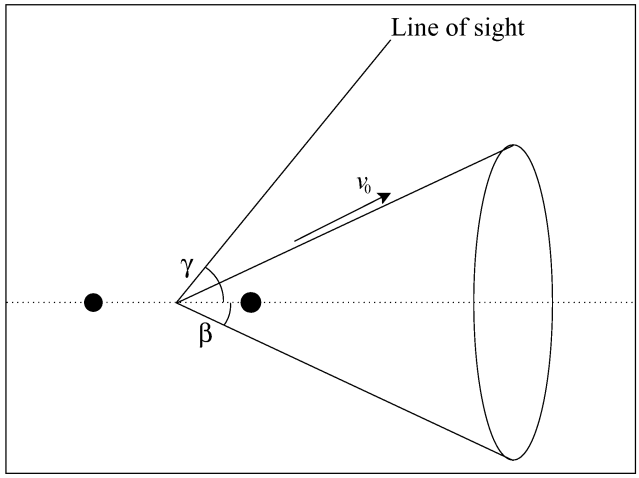

Figure 12. Geometrical model of the wind–wind collision in γ^2 Vel. The solid circles represent the two stars. The cone (with opening half-angle β) represents the wind–wind interaction region (along which X-ray-emitting material is streaming at speed v_0). The viewing angle γ is the angle between the line of sight and the line of centres.

$v^\star$ in his equation (8) (see also his equations 10 and 11). Note that Lührs (1997) does not use γ in his analysis, but instead expresses his velocities in terms of the orbital phase angle and inclination explicitly.

If we identify Δv in equation (10) with the FWHM, then given the mean observed line shift and FWHM ($\bar{v} = -64 \pm 12$ km s^{-1}, FWHM $= 1240 \pm 30$ km s^{-1}; see Section 4.1) and $\gamma = 44°$ (see Section 3.1), we obtain $\beta = 87°$ and $v_0 = 1800$ km s^{-1}. This inferred value of v_0 is rather large, given that the terminal velocity of the WR star wind is 1500 km s^{-1} and the O star wind is likely to be colliding well below its terminal velocity of 2300–2400 km s^{-1}. However, the inferred value of v_0 is sensitive to the relationship between ($v_{\rm max} - v_{\rm min}$) and the FWHM (we have used FWHM $= 0.5\,(v_{\rm max} - v_{\rm min})$ in a rather ad hoc manner to characterize the linewidths), and hence v_0 may in fact be somewhat lower. This is not a problem for β because it is very insensitive to the relationship between ($v_{\rm max} - v_{\rm min}$) and the FWHM.

Note that the mean observed line shift is comparable to the absolute wavelength accuracy of the HETGS (∼100 km s^{-1}; *Chandra* Proposers' Observatory Guide, Section 8.2.4). This means that the measured value of $\bar{v}$ (and hence the derived values of β and v_0) may not be completely trustworthy. However, we can say that $|\bar{v}| < 100$ km s^{-1} (since we would unambiguously be able to detect a larger value of $\bar{v}$). This implies that $\beta > 85°$. The consequences of this are discussed later.

5 LINE PROFILE MODELLING

In an attempt to better understand the line shifts and widths observed in the *Chandra* spectrum of γ^2 Vel, we have calculated model X-ray line profiles using the model described in Henley et al. (2003). This model uses data from a hydrodynamical simulation of the wind–wind collision. The simulations are two-dimensional and assume cylindrical symmetry about the line of centres. The stars' winds are assumed to be spherically symmetric, and orbital effects are assumed to be negligible (this latter assumption is discussed later). The line profiles are calculated by assuming each grid cell produces a thermally Doppler-broadened (i.e. Gaussian) line profile, the amplitude of which depends on the density and temperature of the gas in the cell. The centre of the Gaussian is shifted according to the line-of-sight velocity of gas. Since the simulations assume cylindrical symmetry, each grid cell actually represents a ring of gas. The line-of-sight velocity of the gas varies as a function of position around the ring. This is taken into account by dividing the ring into a number of sections (typically 200), and calculating the contributions from each section (the line-of-sight velocity of a given section depends on the 2-D velocity components in the appropriate hydro grid cell, the viewing angle γ, and the azimuthal angle ϕ of the section around the ring). Absorption by the cold, unshocked winds of the stars is included in the calculations. For each emitting ring section, the integral of the density along the line of sight is calculated (where possible by taking the density directly from the hydro grid; off the grid the density is extrapolated by assuming spherically symmetric winds). This is multiplied by the opacity (calculated for a solar abundance plasma using XSTAR[6]) to give the optical depth τ, and then the amplitude of the Gaussian profile produced by that ring section is multiplied by $e^{-\tau}$. The overall line profile is simply the sum of the contributions from the whole grid (summing over z, r and ϕ).

The major factors that affect X-ray line profiles from colliding wind binaries are the mass-loss rates, the wind speeds, the separation and the viewing angle (i.e. the angle between the line of sight and the line of centres). As the orbit is well determined (Schmutz et al. 1997; de Marco & Schmutz 1999) the separation (0.92–0.94 au) and the viewing angle ($\gamma = 44°$; see Section 4.5) can be specified a priori. The appropriate set of wind parameters to use in the hydrodynamical simulation is less certain. Barlow et al. (1988) measured the terminal velocity of the WR star to be 1520 km s^{-1} from the half-width of the forbidden 12.8-μm [Ne II] emission line. St-Louis et al. (1993) inferred a very similar value (1550 km s^{-1}) from their analysis of phase-varying absorption in *IUE* spectra. Given that the WR star wind is more powerful than the O star wind, the wind–wind collision will be close to the O star. As the separation is ≈60 R_*(WR), the WR star wind is very likely to be at its terminal velocity at the wind–wind collision. Conversely, the O star wind ($v_\infty \approx$ 2300–2400 km s^{-1}; Prinja, Barlow & Howarth 1990; St-Louis et al. 1993) is unlikely to be at its terminal velocity at the wind–wind collision, as evidenced by the disappearance of the high-velocity blue absorption wing from ultraviolet P Cygni profiles obtained by *IUE* when the O star is behind the WR star (St-Louis et al. 1993) and by Willis et al.'s (1995) comparison of model X-ray spectra with their observed *ROSAT* spectra. Note that as the separation varies throughout the orbit, so too will the pre-shock velocities.

As already mentioned in Section 1, Stevens et al. (1996) derived from *ASCA* data a mass-loss rate for the WR star of 3×10^{-5} $M_\odot$ yr^{-1}, a factor of three lower than Barlow et al.'s (1988) radio-determined value of 8.8×10^{-5} $M_\odot$ yr^{-1}, which Stevens et al. (1996) suggested may be due to the fact that radio observations tend to overestimate mass-loss rates when the wind is clumped. It should be noted that both these analyses used larger, pre-*Hipparcos* distances to γ^2 Vel of 460 pc (Barlow et al. 1988) and 450 pc (Stevens et al. 1996). Since the radio-determined mass-loss rate scales as $D^{3/2}$, where D is the distance (Wright & Barlow 1975), using the *Hipparcos* distance of 258 pc (Schaerer et al. 1997) reduces Barlow et al.'s (1988) value to 3.7×10^{-5} $M_\odot$ yr^{-1}. If one assumes the observed X-ray flux scales as $\dot{M}^2$, the mass-loss rate determined using Stevens et al.'s (1996) method scales as D, and so their value reduces

[6] http://heasarc.gsfc.nasa.gov/docs/software/lheasoft/xstar/xstar.html

to 1.7×10^{-5} $M_\odot$ yr^{-1}. More recent values for the mass-loss rate of the WR star (which use the *Hipparcos* distance) include 1.08 or 3.06×10^{-5} $M_\odot$ yr^{-1} based on radio data (assuming a clumped or smooth wind, respectively; Nugis, Crowther & Willis 1998), and 0.93 or 3.3×10^{-5} $M_\odot$ yr^{-1} based on stellar atmosphere modelling of He I and He II lines (the different values coming from different codes and different filling factors; de Marco et al. 2000). However, as noted in Section 3.1, the *Hipparcos* distance has recently been thrown into doubt by the discovery of an association of low-mass, pre-main sequence stars in the direction of γ^2 Vel, and the distance to γ^2 Vel may be between 360 and 490 pc (Pozzo et al. 2000).

For the O star, St-Louis et al. (1993) adopted a typical mass-loss rate for a O9I star (the then accepted spectral classification) of 1.3×10^{-6} $M_\odot$ yr^{-1} (Howarth & Prinja 1989). More recently, de Marco & Schmutz (1999) have derived a much lower $\dot{M}_O$ of 1.8×10^{-7} $M_\odot$ yr^{-1} from hydrodynamical calculations of the radiatively driven wind.

In hydrodynamical simulations of the wind–wind collision in γ^2 Vel, one must take into account radiative cooling. This is because the cooling parameter χ (the ratio of the cooling time-scale to the flow time-scale; Stevens, Blondin & Pollock 1992) is less than unity for the WR star wind. One effect of this is that the wind–wind interaction region can become highly unstable (Stevens et al. 1992), leading to strong time-variability of the calculated line profiles. These instabilities may be partially numerical in origin, and so may lead to unphysical results. Furthermore, if the cooling is very strong, which will be the case for a large adopted mass-loss rate or low wind speed (see equation 8 in Stevens et al. 1992), the shocked gas will collapse into a thin sheet and will not be properly resolved on the grid. This means the model of Henley et al. (2003) cannot be used, as the profiles are calculated after the hydrodynamical simulation and so do not take into account the energy that was radiated during the simulation.

The line profile calculations presented here are based on simulations carried out with the hydrodynamical code COBRA (see, for example, Falle & Komissarov 1996; Pittard et al. 2003), which is second-order accurate in space and time. Radiative cooling is implemented in the simulations. A small amount of numerical viscosity is used to damp the growth of a numerical instability that appears when shocks are stationary on the grid. We adopt mass-loss rates of $\dot{M}_{WR} = 1 \times 10^{-5}$ $M_\odot$ yr^{-1} and $\dot{M}_O = 5 \times 10^{-7}$ $M_\odot$ yr^{-1}, and wind speeds of 1500 km s^{-1} for both winds. For simplicity, we assume the winds are not accelerating, which is why we adopt a wind speed for the O star much lower than its terminal velocity. Fig. 13 shows a density, temperature and speeds map from the resulting simulation. As can be seen, the cooling of the post-shock gas is resolved. Our simulations show little sign of instabilities or post-shock mixing and turbulence. The lack of any instability is unsurprising for two reasons. First, the wind speeds are equal, so there will be very little slip along the contact discontinuity and the Kelvin–Helmholtz instability will not arise. Secondly, the cooling time is long (especially for the O star wind, which remains almost adiabatic), so the shocked gas does not collapse into a thin sheet and the thin-shell instability is not excited. Even if turbulence is present in reality, in order to affect the results discussed below the turbulent velocity would have to be a significant fraction of the bulk flow speed, which is unlikely to be the case.

We have calculated profiles for the Lyα lines and He-like resonance lines of Ne, Mg, Si and S. The line emissivity is assumed to vary just with temperature; we do not, for example, include the enhancement of the He-like resonance line at high densities (Porquet et al. 2001), as it will not be important at the densities present in the

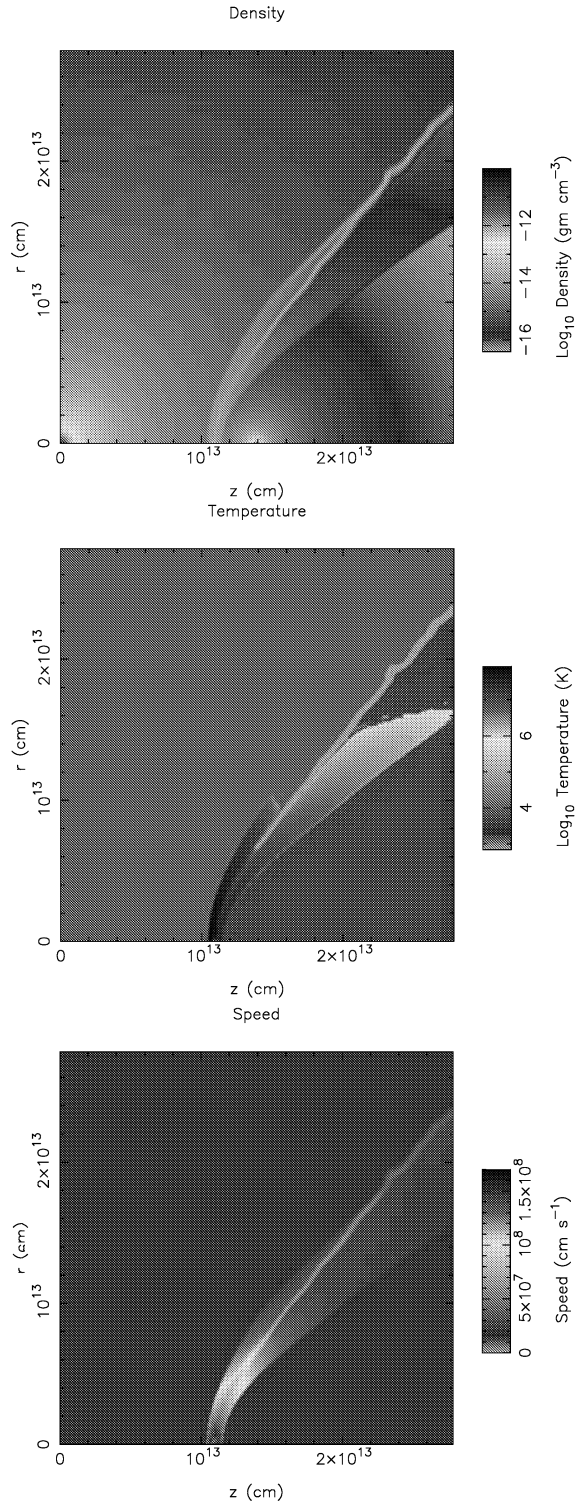

Figure 13. Density (top), temperature (middle) and speed (bottom) maps from a hydrodynamical simulation of γ^2 Vel. The WR star is in the bottom left-hand corner of the grid; the O star is half-way along the bottom axis. The adopted wind parameters are $\dot{M}_{WR} = 1 \times 10^{-5}$ $M_\odot$ yr^{-1}, $\dot{M}_O = 5 \times 10^{-7}$ $M_\odot$ yr^{-1}, $v_{WR} = v_O = 1500$ km s^{-1}.

simulation results. The line emissivities were taken from ATOMDB v1.1.0, which assumes solar abundances. To take into account the different compositions of the winds, we normalize the emission from each wind using the product of the number density of the

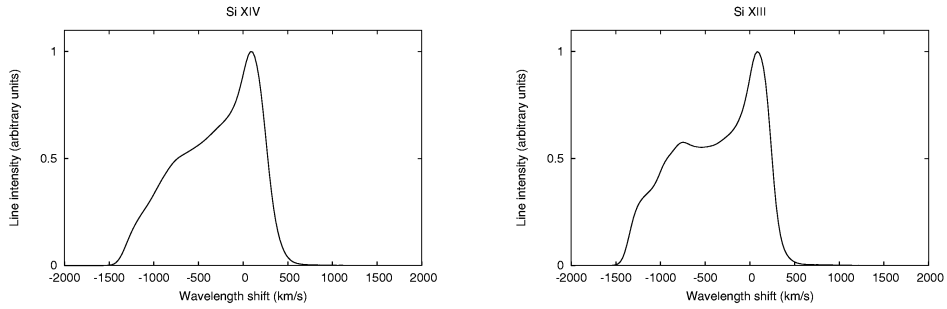

Figure 14. Model Si XIV Lyα (left) and Si XIII resonance (right) line profiles from γ^2 Vel calculated for a viewing angle of $\gamma = 44°$.

element in question and the number density of electrons. The elemental number densities are calculated from the gas density ρ using the elemental mass fractions. For the O star wind we assume solar abundances (Anders & Grevesse 1989), while for the WR wind the mass fractions are calculated using $N(\mathrm{H}) = 0$, $N(\mathrm{C})/N(\mathrm{He}) = 0.14$ (Morris et al. 1999; Schmutz & de Marco 1999), $N(\mathrm{N})/N(\mathrm{He}) = 1.0 \times 10^{-4}$ (Lloyd & Stickland 1999), $N(\mathrm{C})/N(\mathrm{O})/5$ (de Marco et al. 2000), $N(\mathrm{Ne})/N(\mathrm{He}) = 3.5 \times 10^{-3}$ (Dessart et al. 2000) and $N(\mathrm{S})/N(\mathrm{He}) = 6 \times 10^{-5}$ (Dessart et al. 2000). (In the preceding, $N(\mathrm{X})$ denotes the *number* abundance of element X.) The relative abundances of elements more massive than neon are kept at their solar values (Anders & Grevesse 1989). Note that we do not use the elemental abundances measured in Section 3, as the different spectral models used give significantly different abundances for some elements. However, in this case the shapes of the calculated profiles are not very sensitive to the abundances used. The electron density n_e is calculated from the gas density using $\rho = 2\, m_\mathrm{H} n_\mathrm{e}/(1 + X)$, where m_H is the mass of a hydrogen atom and X is the mass fraction of hydrogen (Bowers & Deeming 1984, equations 2.22 and 2.23). Since the line fitting described in Section 4 takes into account the presence of the fainter component of each Lyman line and the intercombination and forbidden lines of the f.i.r. triplets, the lines we calculate are singlets, enabling a direct comparison with the shifts and widths measured from the HETGS spectrum.

Examples of line profiles calculated for $\gamma = 44°$ are shown in Fig. 14, which shows the Si XIII resonance line and the Si XIV Lyα line. The lines are redward-skewed, rather than Gaussian. This skewing is intrinsic and due to the geometry of the emitting region, rather than being due to absorption, which does not have a strong effect on these lines. The lines are broad, each with an FWHM of $\sim$1000 km s^{-1}, in good agreement with the widths measured from the HETGS spectrum. However, the lines are noticeably blueshifted, with centroid shifts of ~ -300 km s^{-1}, in contrast to the essentially unshifted lines in the observed spectrum. The calculated line blueshift decreases as γ increases, but given the opening angle of the shocked region in Fig. 13, increasing γ much above $\sim$40° means the X-ray-emitting plasma would be observed through the WR star wind instead of the O star wind, and this is unlikely given the amount of absorption observed in the spectrum (the column density measured in Section 3 would probably be much larger if the wind–wind collision region were being observed through the WR star wind).

Because the line profile calculations described here are based on 2-D hydrodynamical simulations, they do not take into account the effects of orbital motion on the shape of the wind–wind collision region. However, one can estimate the importance of these effects by assuming the Coriolis force deflects the whole shock cone by some angle $\xi = \tan^{-1}(v_\mathrm{orb}/v_\mathrm{wind})$ in the orbital plane, where v_orb and v_wind are the orbital and wind speeds, respectively. At the time of the *Chandra* observation, the speed of the O star in the rest frame of the WR star was $\approx$200 km s^{-1}. If we assume $v_\mathrm{wind} \approx 1000$ km s^{-1}, we find $\xi \approx 11°$. This means Ψ (see equation 6) is decreased to 25°, and the viewing angle γ decreases to 36°. This actually increases the blueshift that the model predicts to $\sim$350 km s^{-1} (in this case the Coriolis force tends to deflect the shock cone such that there is more gas travelling towards the observer, increasing the predicted blueshift). Using $\gamma = 36°$ instead of 44° in Section 4.5 still predicts a very large shock opening half-angle ($\beta > 86°$). This simple estimate of the size of the effect of the Coriolis force does not take into account the fact that the wind–wind interaction region will change shape, rather than simply being deflected en masse (the whole region becomes bent round into an Archimedean spiral; e.g. Tuthill, Monnier & Danchi 1999). Nevertheless, it appears that Coriolis effects cannot explain the discrepancy between the observed and calculated line shifts.

The discrepancy between the observed and calculated line shifts is most likely due to the opening half-angle of the shocked region being $\sim$40° in our hydrodynamical simulation (see Fig. 13), whereas the simple geometrical model of the emission lines in Section 4.5 implies a shock-cone opening half-angle of >85°. In a CWB with non-accelerating winds, β is a function only of the wind momentum ratio ($\dot{M}_\mathrm{WR} v_\mathrm{WR}/\dot{M}_\mathrm{O} v_\mathrm{O}$). The shock opening angle in our hydrodynamical simulation therefore depends on the adopted values of the wind parameters. However, the shock opening half-angle inferred from our simple geometrical model ($\beta > 85°$) implies approximately equal wind momenta, which is not the case for any sensible set of (constant velocity) wind parameters. We therefore suggest that this large implied opening angle may be evidence of sudden radiative braking (Gayley, Owocki & Cranmer 1997), in which the wind of the WR star is rapidly decelerated when it encounters the radiation field of the O star. Gayley et al. (1997) suggest that the wind–wind collision in γ^2 Vel could be significantly affected by sudden radiative braking, as they find that the wider separation than in V444 Cygni (the main system they study) offers greater opportunities for braking.

6 DISCUSSION

The broad-band X-ray spectrum of γ^2 Vel indicates that a wide range of temperatures is present in the X-ray-emitting plasma, covering a range of $\sim$4–40 MK. The temperature distribution below $\sim$4 MK is poorly contrained, because of the low number of counts above $\sim$14 Å. The differential emission measure (Fig. 5) indicates the temperature distribution falls off above $\sim$40 MK. This temperature range implies shock speeds of 500–1700 km s^{-1} assuming solar abundances, or 300–1100 km s^{-1} assuming WC8 abundances. The upper values of these ranges are reasonable given the discussion of

wind speeds in the previous section. The post-shock temperature corresponding to $v_\infty(\mathrm{O}) = 2400$ km s^{-1} is 80 MK. The lack of any evidence for gas at such high temperatures suggests that the O star wind is not colliding at its terminal velocity near the line of centres – the shocked gas near the line of centres is the densest in the collision region, and so if there is any very hot (∼80 MK) gas it should make a significant contribution to the X-ray emission. However, it should be noted that the sensitivity of the HETGS falls off at short wavelengths ($\lambda \lesssim 2$ Å) and so it is less sensitive to emission from very hot gas. To investigate this further, we synthesized a spectrum by adding a 80-MK `apec` component to our best-fitting 2T `apec` model (model B in Table 1). With its emission measure [expressed in terms of the helium density (EM $= \int n_\mathrm{e} n_\mathrm{He}\, \mathrm{d}V$), because of the lack of hydrogen in the WR star wind] fixed at 2×10^{53} cm^{-3}, this model leads to significant Fe XXV emission near 1.85 Å which is not observed. This implies that the emission measure of the very hot (80-MK) gas is at least a factor of 5 smaller than those of the two `apec` components in Table 1.

The lower limits of the implied shock speeds do not imply low wind speeds *per se*, but instead that parts of the wind are being shocked obliquely as is expected from the geometry of the wind–wind collision region. This oblique shocking also explains (at least qualitatively) the shape of the DEM in Fig. 5. If all the gas were being shock-heated to ∼40 MK at the shock apex and then allowed to cool radiatively, one would expect the DEM to have a shape that is the inverse of the cooling function, i.e. at temperatures where the cooling function is low, there will be more gas (as it will take longer for gas to cool through this temperature) and so a larger emission measure (and vice versa). Therefore, one would expect the emission measure to decrease from ∼20 MK to lower temperatures (see, for example, fig. 3 in Antokhin, Owocki & Brown 2004). Instead, the observed emission measure rises from ∼20 to ∼8 MK. This means that gas is being fed in at lower temperatures, which is consistent with the oblique shocking that occurs away from the line of centres.

The column density derived from the broad-band fitting ($N_\mathrm{H} \approx 2 \times 10^{22}$ cm^{-2}) is consistent with that measured by Rauw et al. (2000) from an *ASCA* observation at the same phase ($N_\mathrm{H} = 2.4 \times 10^{22}$ cm^{-2} at $\Phi = 0.078$). The measured value indicates the wind–wind interaction region is being observed through the wind of the O star, which is what is expected given the viewing orientation.

As has already been stated, the broad-band spectral models used in Section 3 give poor fits to the data ($\chi^2_\nu \sim 2$). Furthermore, they can at best only characterize the general properties of the X-ray-emitting plasma. A better approach is to calculate the X-ray emission expected from the hydrodynamics of the wind–wind collision. This may be done using numerical hydrodynamical simulations (e.g. Stevens et al. 1996), in a similar fashion to the method used in Section 5. An alternative is to use the semi-analytical approach devised by Antokhin et al. (2004). First, the shape of the interaction region is calculated using wind momentum balance. The shocks are assumed to be highly radiative, so the shocked material collapses into a thin layer and the two shocks and the contact discontinuity (CD) are treated as effectively synonymous. At the shocks (which are treated as locally planar), the wind is shock-heated to some temperature T_s and then cools rapidly (effectively to $T = 0$) in a thin layer between the shock and the CD; i.e. all the kinetic energy associated with the velocity component locally perpendicular to the shock is radiated away. The former approach works best for adiabatic shocks (the instabilities of radiative shocks lead to substantial mixing between hot and cold material, the physically appropriate degree of which is difficult to predict a priori), whereas Antokhin et al. 's (2004) method assumes fully radiative shocks. In γ^2 Vel, the O star wind is effectively adiabatic, and while the WR star wind is radiative, it is not highly radiative (the post-shock cooling is resolved in Fig. 13). Nevertheless, a useful next step in our understanding will be the application of both methods to the *Chandra* HETGS spectrum of γ^2 Vel. Since velocity information is available when synthesizing spectra using either method, it should also be possible to calculate line shapes self-consistently. Both methods may be used to generate grids of spectra for a range of parameters (e.g. $\dot{M}$, v_∞). These can then be fitted to the spectra in order to constrain wind parameters. In order to fit to the wealth of detail in the HETGS spectrum, the most up-to-date atomic data available must be used to synthesize the spectra. However, such an analysis is beyond the scope of the current paper.

From the emission lines in the X-ray spectrum, we measured temperatures by comparing the fluxes of lines from H-like and He-like ions of a given element, and by using G ratios derived from He-like f.i.r. triplets. For Ne and Mg, the temperatures measured by the two methods are in good agreement with each other. However, the Si XIV:Si XIII flux ratio implies a significantly higher temperature (12 MK) than the Si XIII G ratio (5 MK). As already stated, this may simply indicate that the Si XIII (ionization potential (I.P.) = 2.438 keV; Däppen 2000) originates from somewhat cooler regions than the Si XIV emission (I.P. = 2.673 keV). However, it could also be evidence of non-equilibrium ionization (NEI). This could tie in with the evidence that the Mg XI emission (I.P. = 1.7618 keV) seems to originate closer to the O star than the Si XIII emission, as evidenced by the R ratios derived from their He-like f.i.r. triplets. Furthermore, the G ratios indicate that the Mg XI emission originates from hotter gas ($T_e = 7$ MK) than the Si XIII emission ($T_e = 5$ MK). This implies it originates nearer the line of centres (and hence nearer the O star), as the temperature decreases monotonically away from the line of centres (see Fig. 13). This is counter to what is expected if collisional ionization equilibrium holds, as in that case the Mg XI emission would originate in cooler gas further from the line of centres than the Si XIII emission.

One can assess whether or not NEI is important in a colliding wind binary by deriving an ionization parameter ψ analogous to the cooling parameter χ of Stevens et al. (1992). In the adiabatic limit, NEI effects will be important if the ionization equilibration time-scale is larger than the flow time-scale, whereas in the radiative limit they will be important if the ionization equilibration time-scale is larger than the cooling time-scale. The ionization equilibration time-scale t_Ieq is given by (Masai 1994)

$$t_\mathrm{Ieq} = \frac{10^{12}\ \mathrm{cm}^{-3}\ \mathrm{s}}{n_\mathrm{e}}, \tag{11}$$

where n_e is the electron number density. For the flow time-scale t_flow we shall use

$$t_\mathrm{flow} = \frac{d}{c_\mathrm{s}}, \tag{12}$$

where d is the distance from the star to the contact discontinuity and c_s is the post-shock sound speed (Stevens et al. 1992). The cooling time-scale t_cool is given approximately by (Stevens et al. 1992)

$$t_\mathrm{cool} = \frac{kT}{4n\Lambda(T)}, \tag{13}$$

where T is the post-shock temperature, n is the number density of the wind at the shock and Λ is the cooling function ($\approx 2 \times 10^{-23}$ erg s^{-1} cm^3 for solar-abundance material; see fig. 10 in Stevens et al. 1992).

Note that t_flow in equation (12) is the time-scale for the post-shock gas to travel a distance $\sim d$ away from the line of centres, whereas

the temperature in the post-shock gas may decrease away from the line of centres such that the ionization balance for a given element is expected to go from being dominated by H-like ions to being dominated by He-like ions in a distance less than d. It is therefore possible that the above flow time-scale is too long to be appropriate. Nevertheless, with this choice of $t_{\rm flow}$ one finds that in the adiabatic limit

$$\psi_{\rm adiabatic} \equiv \frac{t_{\rm leq}}{t_{\rm flow}} = 0.02 \mu_{\rm e} \frac{d_{12} v_8^2}{\dot{M}_{-7}}, \quad (14)$$

whereas in the radiative limit

$$\psi_{\rm radiative} \equiv \frac{t_{\rm leq}}{t_{\rm cool}} = 0.03 \frac{\mu_{\rm e}}{\mu^2} \frac{1}{v_8^2}, \quad (15)$$

where $\mu_{\rm e}$ is the average mass *per electron* in a.m.u. (1.2 for solar abundance material and 2 for WC material), μ is average mass *per particle* in a.m.u. (0.61 for solar abundance material and 1.5 for WC material), d_{12} is the distance from the star to the contact discontinuity in units of 10^{12} cm, v_8^2 is the wind speed in units of 1000 km s^{-1}, and $\dot{M}_{-7}$ is the mass-loss rate in units of 10^{-7} M$_\odot$ yr^{-1}. If $\psi \ll 1$ then collisional ionization equilibrium holds.

To determine ψ we assume $\dot{M}_{\rm WR} = 3 \times 10^{-5}$ M$_\odot$ yr^{-1}, $\dot{M}_{\rm O} = 5 \times 10^{-7}$ M$_\odot$ yr^{-1} and $v_{\rm WR} = v_{\rm O} = 1500$ km s^{-1}, and calculate d_{12}(WR) and d_{12}(O) by assuming ram pressure balance at the contact discontinuity (Stevens et al. 1992). Using equation (14), we find $\psi_{\rm WR} = 0.004$ and $\psi_{\rm O} = 0.02$, whereas equation (15) gives $\psi_{\rm WR} = 0.01$ and $\psi_{\rm O} = 0.04$. Note that the value of $\psi_{\rm WR}$ in the radiative limit is probably underestimated by a factor of a few, because Λ is larger for WC material than solar abundance material (see fig. 10 in Stevens et al. 1992). The winds in γ^2 Vel are neither adiabatic nor completely radiative, and so the true values of $\psi_{\rm WR}$ and $\psi_{\rm O}$ lie between the above values. This therefore suggests that collisional ionization equilibrium should hold for both stars' winds in γ^2 Vel, in contrast to what we infer from the Mg XI and Si XIII f.i.r. triplets. A detailed self-consistent calculation of the ionization balance in the wind–wind collision is needed to resolve this issue.

As well as inferring the temperatures and locations of different regions of X-ray-emitting plasma from the emission line spectrum, we have used the line shifts and widths to infer the geometry of the wind–wind collision. The essentially unshifted lines imply a large shock-cone opening half-angle $\beta > 85^\circ$. As stated previously, this may be evidence of sudden radiative braking (Gayley et al. 1997). Note that the calculation that leads to this opening angle does not take into account absorption in the cool, unshocked wind of the O star, which can have a profound affect on the shape of the X-ray emission lines (Henley et al. 2003). However, the calculations in Section 5, while they do not reproduce the observed line shifts, do indicate that absorption does not have a strong effect on the line profiles in γ^2 Vel.

Earlier observations of γ^2 Vel, however, do not imply such a wide shock opening half-angle. From the duration of the period of enhanced emission in the *ROSAT* light curve, Willis et al. (1995) infer a shock opening half-angle of $\sim 25^\circ$. Their estimate implicitly assumes an inclination of 90°, but even using the inclination we have adopted throughout this paper ($i = 63^\circ$; de Marco & Schmutz 1999) only increases the inferred half-angle to $\sim 50^\circ$. Furthermore, if the shock opening half-angle is as large as 85°, Rauw et al.'s (2000) *ASCA* observation at phase $\Phi = 0.978$ would have seen the wind–wind collision through the O star wind, and their measured column density would have been similar to that which they measured for their $\Phi = 0.078$ observation ($N_{\rm H} = 2.4 \times 10^{22}$ cm^{-2}), rather than three times larger ($N_{\rm H} = 7.5 \times 10^{22}$ cm^{-2}).

This discrepancy between the shock opening angle inferred from the line shifts and the previous X-ray observations of γ^2 Vel leads one to speculate that the intrinsic emission of the O star is contributing a significant amount to the observed X-ray spectrum (the WR star is unlikely to contribute any intrinsic emission, as no single WC star has ever been convincingly detected in X-rays; Oskinova et al. 2003). The standard wind-shock model, with X-rays being emitted from shocks distributed throughout the wind due to instabilities in the line-driving force (e.g. Owocki et al. 1988), predicts broad, blueshifted, blue-skewed line profiles (Ignace 2001; Owocki & Cohen 2001), as the redshifted emission from the far side of the wind is attenuated by the wind. Such profiles have been observed from the well-studied O4f star ζ Pup (Cassinelli et al. 2001), and have been successfully fitted with a simple model of wind absorption (Kramer, Cohen & Owocki 2003), but in general a clear picture of X-ray line emission from early-type stars has yet to emerge. The models for X-ray line profiles from single O stars discussed above cannot be applied to γ^2 Vel because they rely upon spherical symmetry, which is not the case in γ^2 Vel because of the wind–wind collision. However, if the lines were coming from the O star wind, the FWHM (1200 km s^{-1}) implies that most of the emission originates from where the line-of-sight velocity is between -600 and $+600$ km s^{-1} (i.e. from where $|v| \lesssim v_\infty/4$). If one assumes a β velocity law of the form $v(r) = v_\infty(1 - R_*/r)^\beta$ with $\beta = 0.8$ (St-Louis et al. 1993), this implies the line emission mostly originates less than 1.2 R_*(O) from the centre of the O star, which is inconsistent with the minimum radii of formation inferred from the R ratios of He-like ions. Of course, this argument says nothing about the lines from H-like ions, but given that the widths and shifts are similar for all ions (Fig. 8), it is reasonable to assume a common origin for all the lines.

The $L_{\rm X}/L_{\rm bol}$ ratio could be used to assess the importance of the O star's intrinsic emission to the total emission observed from γ^2 Vel. Pollock (1987) measured $L_{\rm X}/L_{\rm bol} = 0.44 \times 10^{-7}$ for γ^2 Vel with *Einstein*, which is typical for lone O stars ($L_{\rm X}/L_{\rm bol} \sim 10^{-7}$; Chlebowski 1989; Moffat et al. 2002). Model B in Table 1 gives an intrinsic X-ray luminosity in the *Einstein* (0.2–3.5 keV) band of 9.6×10^{32} erg s^{-1}. Using $L_{\rm bol}$(O) $= 2.1 \times 10^5$ L$_\odot$ (de Marco & Schmutz 1999) gives $L_{\rm X}/L_{\rm bol} = 12 \times 10^{-7}$, which is much higher than the *Einstein* value and which seems to indicate that colliding wind emission dominates. Unfortunately, owing to the low number of counts at low energies, the luminosity at lower energies is very poorly constrained, and so this conclusion may be unreliable. However, the high temperatures inferred from the spectrum (up to $\sim$40 MK) are evidence of colliding wind emission, as the standard wind-shock model does not produce strong enough shocks to produce such high temperatures.

7 SUMMARY

We have carried out a new analysis of an archived *Chandra* HETGS spectrum of γ^2 Vel. As with the previously published analysis (Skinner et al. 2001) we find the lines are essentially unshifted, with a mean FWHM of 1240 ± 40 km s^{-1}. The lack of strong absorption means the line-of-sight is through the O star wind. We find a wide range of temperatures is present in the X-ray-emitting plasma, from $\sim$4 to $\sim$40 MK, which is in good agreement with the range of temperatures expected from a hydrodynamical simulation of the wind–wind collision. However, line profile calculations based on such simulations imply the lines should be blueshifted by a few hundredkm s^{-1}. We suggest that the unshifted lines may imply a wider shock opening half-angle ($> 85^\circ$) than that which is seen in

the hydrodynamical simulations. This may be evidence of sudden radiative braking. However, such a wide shock opening half-angle seems to disagree with earlier *ROSAT* and *ASCA* observations of γ^2 Vel. A full radiation hydrodynamics simulation of γ^2 Vel is needed to investigate what effect radiative braking has on the morphology of the wind–wind collision and how the degree of this effect may change with orbital separation (see Pittard 1998).

Unlike Skinner et al. (2001), we find evidence that the Mg XI emission emerges from hotter gas closer to the O star than the Si XIII emission, which may be evidence of non-equilibrium ionization. Future work will include trying to model the ionization balance in colliding wind binaries self-consistently. This may be important for the study of other colliding wind systems, such as WR140 (Pollock et al. 2004).

Gayley et al. (1997) point out that the eccentricity of γ^2 Vel allows the degree of braking to be studied as a function of the orbital separation. Unfortunately, the strong absorption in the WR star wind means that a long (∼200 ks) *Chandra* pointing would be needed to obtain a high-quality spectrum at phases other than when the O star is in front. However, γ^2 Vel is an ideal target for *Astro-E2*, due to its greater effective area at higher energies. We have proposed a 75-ks *Astro-E2* observation of γ^2 Vel when the O star is not in front (PI: D. Henley). This will enable us to measure line shifts and widths at a different orbital phase from the *Chandra* observation. From this we can investigate how the shock opening angle varies with orbital phase. By comparing this with the shock opening angle inferred from radiation hydrodynamics simulations, we will be able to place constraints on the coupling between the O star radiation field and the WR star wind, which will in turn provide insights into the poorly understood physics of WR wind driving.

ACKNOWLEDGMENTS

DBH gratefully acknowledges funding from the School of Physics and Astronomy, University of Birmingham. We would like to thank Andy Pollock for useful discussions on emission line fitting, and the referee, David Cohen, whose comments have significantly improved this paper. This research has made use of the SIMBAD data base, operated at CDS, Strasbourg, France. This research has also made use of the *Chandra* Data Archive (CDA), part of the *Chandra* X-Ray Observatory Science Centre is operated for NASA by the Smithsonian Astrophysical Observatory.

REFERENCES

Anders E., Grevesse N., 1989, Geochim. Cosmochim. Acta, 53, 197
Antokhin I. I., Owocki S. P., Brown J. C., 2004, ApJ, 611, 434
Barlow M. J., Roche P. F., Aitken D. K., 1988, MNRAS, 232, 821
Blumenthal G. R., Drake G. W. F., Tucker W. H., 1972, ApJ, 172, 205
Bowers R., Deeming T., 1984, Astrophysics I: Stars. Jones and Bartlett, Sudbury, MA
Cash W., 1979, ApJ, 228, 939
Cassinelli J. P., Miller N. A., Waldron W. L., MacFarlane J. J., Cohen D. H., 2001, ApJ, 554, L55
Cherepashchuk A. M., 1976, SvA Lett., 2, 138
Chlebowski T., 1989, ApJ, 342, 1091
Cohen D. H., Cooper R. G., Macfarlane J. J., Owocki S. P., Cassinelli J. P., Wang P., 1996, ApJ, 460, 506
Conti P. S., Smith L. F., 1972, ApJ, 172, 623
Däppen W., 2000, in Cox A. N., ed., Allen's Astrophysical Quantities, fourth edn. Springer-Verlag, New York
de Marco O., Schmutz W., 1999, A&A, 345, 163
de Marco O., Schmutz W., Crowther P. A., Hillier D. J., Dessart L., de Koter A., Schweickhardt J., 2000, A&A, 358, 187
Dessart L., Crowther P. A., Hillier D. J., Willis A. J., Morris P. W., van der Hucht K., 2000, MNRAS, 315, 407
Falle S. A. E. G., Komissarov S. S., 1996, MNRAS, 278, 586
Gabriel A. H., Jordan C., 1969, MNRAS, 145, 241
Gayley K. G., Owocki S. P., Cranmer S. R., 1997, ApJ, 475, 786
Gorenstein P., 1975, ApJ, 198, 95
Henley D. B., Stevens I. R., Pittard J. M., 2003, MNRAS, 346, 773
Howarth I. D., Prinja R. K., 1989, ApJS, 69, 527
Huenemoerder D. P., Canizares C. R., Schulz N. S., 2001, ApJ, 559, 1135
Ignace R., 2001, ApJ, 549, L199
Kramer R. H., Cohen D. H., Owocki S. P., 2003, ApJ, 592, 532
Lloyd C., Stickland D. J., 1999, in van der Hucht K. A., Koenigsberger G., Eenens P. R. J., eds, Proc. IAU Symp. 193, Wolf–Rayet Phenomena in Massive Stars and Starburst Galaxies, p. 362
Lührs S., 1997, PASP, 109, 504
Masai K., 1994, ApJ, 437, 770
Moffat A. F. J. et al., 2002, ApJ, 573, 191
Morris P. W., van der Hucht K. A., Willis A. J., Dessart L., Crowther P. A., Williams P. M., 1999, in van der Hucht K. A., Koenigsberger G., Eenens P. R. J., eds, Proc. IAU Symp. 193, Wolf–Rayet Phenomena in Massive Stars and Starburst Galaxies, p. 77
Morrison R., McCammon D., 1983, ApJ, 270, 119
Nugis T., Crowther P. A., Willis A. J., 1998, A&A, 333, 956
Oskinova L. M., Ignace R., Hamann W.-R., Pollock A. M. T., Brown J. C., 2003, A&A, 402, 755
Owocki S. P., Cohen D. H., 2001, ApJ, 559, 1108
Owocki S. P., Castor J. I., Rybicki G. B., 1988, ApJ, 335, 914
Paerels F. B. S., Kahn S. M., 2003, ARA&A, 41, 291
Pittard J. M., 1998, MNRAS, 300, 479
Pittard J. M., Dyson J. E., Falle S. A. E. G., Hartquist T. W., 2003, A&A, 408, 79
Pollock A. M. T., 1987, ApJ, 320, 283
Pollock A. M. T., Corcoran M. F., Stevens I. R., Williams P. M. 2004, ApJ, submitted
Porquet D., Mewe R., Dubau J., Raassen A. J. J., Kaastra J. S., 2001, A&A, 376, 1113
Pozzo M., Jeffries R. D., Naylor T., Totten E. J., Harmer S., Kenyon M., 2000, MNRAS, 313, L23
Prinja R. K., Barlow M. J., Howarth I. D., 1990, ApJ, 361, 607
Rauw G., Stevens I. R., Pittard J. M., Corcoran M. F., 2000, MNRAS, 316, 129
Schaerer D., Schmutz W., Grenon M., 1997, ApJ, 484, L153
Schmutz W., de Marco O., 1999, in van der Hucht K. A., Koenigsberger G., Eenens P. R. J., eds, Proc. IAU Symp. 193, Wolf–Rayet Phenomena in Massive Stars and Starburst Galaxies, p. 147
Schmutz W. et al., 1997, A&A, 328, 219
Skinner S. L., Güdel M., Schmutz W., Stevens I. R., 2001, ApJ, 558, L113
Smith R. K., Brickhouse N. S., 2000, Rev. Mex. Astron. Astrofis. Ser. Conf., 9, 134
Smith R. K., Brickhouse N. S., Liedahl D. A., Raymond J. C., 2001, ApJ, 556, L91
St-Louis N., Willis A. J., Stevens I. R., 1993, ApJ, 415, 298
Stevens I. R., Blondin J. M., Pollock A. M. T., 1992, ApJ, 386, 265
Stevens I. R., Corcoran M. F., Willis A. J., Skinner S. L., Pollock A. M. T., Nagase F., Koyama K., 1996, MNRAS, 283, 589
Tuthill P. G., Monnier J. D., Danchi W. C., 1999, Nat, 398, 487
van der Hucht K. A., 2001, NewAR, 45, 135
Willis A. J., Schild H., Stevens I. R., 1995, A&A, 298, 549
Wojdowski P. S., Schulz N. S., 2004, ApJ, submitted (astro-ph/0403603)
Wright A. E., Barlow M. J., 1975, MNRAS, 170, 41

This paper has been typeset from a TEX/LATEX file prepared by the author.